^{99m}Tc-IgG$_3$ {[^{99m}Tc](HYNIC-anti-MT1-MMP)(tricine)$_2$ and [^{99m}Tc](HYNIC-IgG$_3$)(tricine)$_2$, respectively}. After 3 h at room temperature, the radiolabelled products were purified by SE chromatography on a PD-10 desalting column (Amersham Biosciences AB, Uppsala, Sweden) using 0.05 M phosphate-buffered saline (PBS) (pH 7.0). The radiochemical purities of ^{99m}Tc-MT1-MMP mAb and ^{99m}Tc-IgG$_3$ were determined by another SE column filtration (PD-10 column) in each preparation and found to be 92.3±1.5% and 92.3±5.5%, respectively.

Animals

Three male Japanese White (JW) rabbits (3 months old, Biotek Inc., Saga, Japan) were used to obtain peritoneal macrophages. For non-invasive imaging and biodistribution studies of ^{99m}Tc-MT1-MMP mAb, four male WHHLMI rabbits (11–18 months old: 3.4±0.4 kg body weight) that were bred at Kobe University were used. Four JW rabbits (3 months old: 2.2±0.1 kg body weight, Biotek Inc., Saga, Japan) were used as controls. Four WHHLMI rabbits (two male and two female, 10–15 months old, 2.9±0.3 kg) were used for non-invasive imaging and biodistribution studies of ^{99m}Tc-IgG$_3$. The animals were fed standard chow (type CR-3, Clea Japan Inc., Tokyo, Japan) at 120 g/day and were given water ad libitum. All animal procedures were approved by the Kyoto University Animal Care Committee.

Immunoreactivity of HYNIC-MT1-MMP mAb

Rabbit peritoneal macrophages were obtained by the method of Ishii et al. [24], with minor modifications. The cells were suspended in medium A [Dulbecco's modified Eagle's medium containing 1 mM glutamine, penicillin (100 U/ml), streptomycin (100 μg/ml) and 0.2% lactalbumin hydrolysate] at a final concentration of 2.5×10^6 cells/ml. Aliquots of the cell suspension were placed into plastic Petri dishes and cultured in a humidified 5% CO_2 incubator at 37°C. After 2 h, each dish was washed twice with medium A and then cultured for a further 18 h. Cells (1×10^6 cells) were incubated with MT1-MMP mAb (50 μg/ml, 100 μl), HYNIC-MT1-MMP mAb (50 μg/ml, 100 μl) or control mouse IgG$_3$ (50 μg/ml, 100 μl) for 30 min at 4°C, followed by incubation with 10 μg/ml of Alexa Fluor® 488 goat anti-mouse IgG (100 μl, Molecular Probes, Inc., Eugene, OR, USA). For flow cytometry analysis, cells were mixed with IsoFlow solution (Beckman Coulter Inc., Fullerton, CA, USA) and immediately analysed by a FACScan instrument (Becton Dickinson Inc., Franklin Lakes, NJ, USA). Immunoreactivity of HYNIC-MT1-MMP mAb was evaluated with the median fluorescence intensity ratio to control mouse IgG$_3$ and compared with that of MT1-MMP mAb. Measurements were performed three times per rabbit using three JW rabbits.

Non-invasive imaging

After 12 h of fasting, rabbits were initially anaesthetized with ketamine (35 mg/kg, intramuscularly) and xylazine (5 mg/kg, intramuscularly). The anaesthetic state was maintained with additional doses of ketamine and xylazine during the experimental period. Rabbits were placed on the scanner bed in a prone position to include the abdominal aorta in the field of view. ^{99m}Tc-MT1-MMP mAb (140–741 MBq, 300 μg) was injected into the marginal ear vein of four WHHLMI rabbits and four control rabbits. At 10 min and 24 h after injection of the radiotracer, planar images were obtained for 10 min with a gamma camera (SPECT 2000H, Hitachi Medical Co., Tokyo, Japan) employing a low energy high resolution parallel-hole collimator with a spatial resolution of 6.7 mm in full-width at half-maximum (FWHM). Serial arterial blood samples were collected from an auricular artery. Similarly, imaging studies of ^{99m}Tc-IgG$_3$ were performed after the injection of ^{99m}Tc-IgG$_3$ (91–198 MBq, 300 μg) into the marginal ear vein of four WHHLMI rabbits. All rabbits were also applied to the biodistribution studies described below.

Biodistribution studies

Immediately after the non-invasive imaging studies, 24 h after tracer injection, the animals were sacrificed with an overdose of pentobarbital. The ascending-arch, thoracic and abdominal aortas, blood and other tissues were removed. The ascending-arch aortas were divided into six segments, while the thoracic and abdominal aortas were divided into nine segments (Fig. 1). Each segment was weighed and immediately fixed in a solution containing L-(+)-lysine hydrochloride (75 mM) and 4% paraformaldehyde in phosphate buffer (37.5 mM, pH 7.4). The radioactivity of each sample was measured with a well-type gamma counter (ARC-2000, Aloka, Tokyo, Japan). Results were expressed as the differential uptake ratio (DUR), which was calculated as (tissue activity/tissue weight)/(injected radiotracer activity/animal body weight), with activities given in becquerels and weights given in grams. The aorta to blood ratio (A/B ratio) and the aorta to muscle ratio (A/M ratio) were calculated from DUR values.

Autoradiography (ARG)

Autoradiographic studies were also performed using the aortas obtained at 24 h after tracer injection (the same aortas used in the biodistribution studies). A total of eight

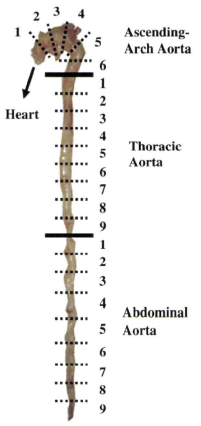

Fig. 1 Segmentation of the ascending-arch, thoracic and abdominal aortas. The ascending-arch aortas were divided into six segments, while the thoracic and abdominal aortas were divided into nine segments

segments, the second and fifth segments from the ascending-arch aorta, and the second, fifth and eighth segments from the thoracic and abdominal aortas, from each animal were used for autoradiographic studies. These segments were frozen and cut into 20-μm thick slices using a cryomicrotome. To obtain ^{99m}Tc-MT1-MMP mAb and ^{99m}Tc-IgG$_3$ autoradiograms, sections were thaw-mounted on silane-coated slides, which were then placed on a phosphor image plate (Fuji Imaging Plate BAS-UR, Fuji Photo Film, Tokyo, Japan) for 24 h together with calibrated standards ($^{99m}TcO_4^-$solution). The ARG images were analysed using a computerized imaging analysis system (Bio-Imaging Analyzer BAS2500 and Image Gauge Software, Fuji Photo Film, Tokyo, Japan). Radioactivity in each region of interest (ROI) was expressed as %ID×BW/mm^2, calculated as (radioactivity in ROI)/(injected radioactivity/animal body weight), with radioactivity in ROI given in becquerels/mm^2, injected activity given in becquerels and weight given in grams.

Histological analysis

Serial sections of ARG slices were subjected to histological analysis. Azan-Mallory staining, haematoxylin and eosin (H&E) staining and immunohistochemical staining (MT1-MMP, macrophage and smooth muscle cell) were performed. Immunohistochemical staining of MT1-MMP was carried out using the anti-MT1-MMP monoclonal IgG (MT1-MMP mAb, described above) and a Dako EnVision + kit (Dako, Tokyo, Japan) with haematoxylin counterstaining. In the same manner, immunohistochemical staining for macrophages and smooth muscle cells was carried out with a rabbit macrophage-specific mAb, RAM11 (Dako, Tokyo, Japan) and a human smooth muscle actin-specific mAb, 1A4 (Dako, Tokyo, Japan), respectively. Immunostaining with subclass-matched irrelevant IgG served as a negative control. Azan-Mallory staining and H&E staining were performed with standard procedures. Areas (μm^2) occupied by each lesion component were evaluated with a VHX Digital Microscope (Keyence Corp., Osaka, Japan). Collagen-rich fibres and extracellular lipid deposits (extracellular vacuoles and lacunae) were assessed with Azan-Mallory staining. Macrophage and smooth muscle cell areas were determined by immunohistochemical staining (RAM11 and 1A4). MT1-MMP expression density was assessed as a percentage of positively stained areas (% positive).

Classification of atherosclerotic lesions

The atherosclerotic lesions in WHHLMI rabbits were divided into four categories using a classification scheme based on the recommendations of the American Heart Association (AHA) [25, 26] by Azan-Mallory staining and H&E staining as previously described [27, 28] (Fig. 2a–p): (1) neointimal lesion (type I–III), (2) atheromatous lesion (type IV), (3) fibroatheromatous lesion (type Va, Vb) and (4) collagen-rich lesion (type Vc). Neointimal lesions were defined as having adaptive thickening of the intima consisting of mainly smooth muscle cells and few macrophages. Atheromatous lesions contained thin fibrous connective tissue and a dense accumulation of extracellular lipid and foam cells and were considered to be vulnerable-like lesions in human atherosclerotic plaques. Fibroatheromatous lesions were composed of several lipid cores, separated by thick layers of fibromuscular connective tissue, which was relatively stable to rupture [29]. Collagen-rich lesions consisted of a predominantly collagenous component and contained smooth muscle cells.

ROIs were placed to cover each atherosclerotic lesion in the aorta section of the WHHLMI rabbit and then transferred to the corresponding ARG images (Fig. 2q–v).

Statistical analysis

Data are presented as the mean ± SD. Statistical analysis was performed with the Kruskal-Wallis test with post hoc analysis by the Holm test (Table 1). Correlation coefficients were assessed by Spearman rank correlation coefficients (Fig. 4i, j). Comparisons among lesion types were performed using the Kruskal-Wallis test with post hoc analysis by the Holm test (Fig. 5a, b). A two-tailed value of $p<0.05$ was considered statistically significant.

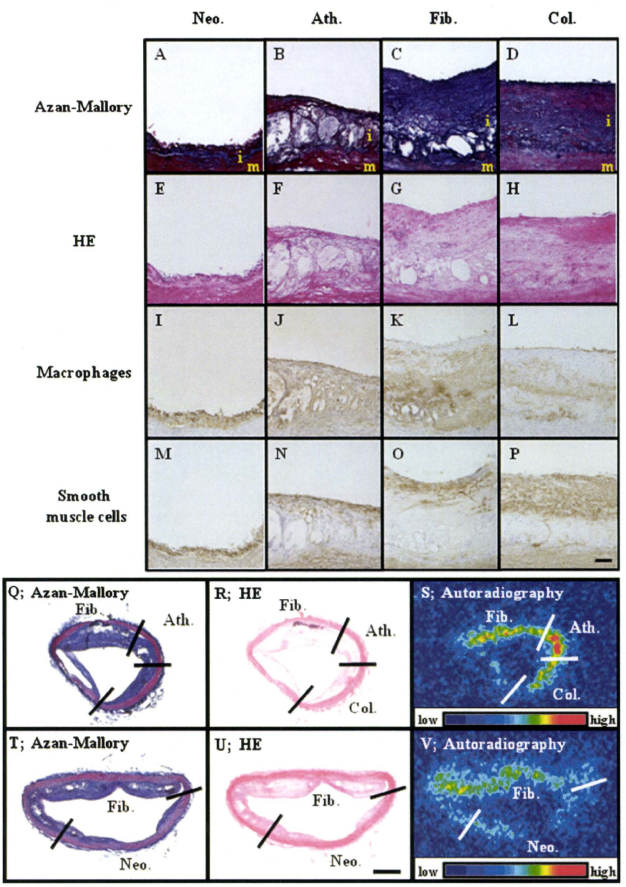

Fig. 2 Representative photomicrographs of histological features (**a**–**p**) and lesion classification (**q**–**v**) of atherosclerotic lesions in WHHLMI rabbits. Atherosclerotic lesions were microscopically divided into four categories as described in the "Materials and methods" section: neointimal lesion (*Neo.*, *left column*), atheromatous lesion (*Ath.*, *second column*), fibroatheromatous lesion (*Fib.*, *third column*) and collagen-rich lesion (*Col.*, *right column*). ROIs were placed to cover each atherosclerotic lesion in the aorta section of the WHHLMI rabbit and then transferred to the corresponding ARG images. *m* media, *i* intima, *bar* = 100 μm (**a**–**p**) and 1 mm (**q**–**v**)

Results

Immunoreactivity of HYNIC-MT1-MMP mAb

By FACS analysis, the signals of MT1-MMP mAb and HYNIC-MT1-MMP mAb were clearly distinct from that of the negative control IgG_3. The median fluorescence intensity ratios of MT1-MMP mAb and HYNIC-MT1-MMP mAb to control IgG_3 were 2.99±0.26 and 2.36±0.92, respectively, and the difference was not statistically significant (Kruskal-Wallis test).

Non-invasive imaging and biodistribution studies

Planar images showed primarily blood pool radioactivity in the abdominal aorta of every rabbit at 10 min after injection of ^{99m}Tc-MT1-MMP mAb or ^{99m}Tc-IgG_3 (Fig. 3a–c). At 24 h, the atherosclerotic abdominal aorta was clearly visible in the WHHLMI rabbits given ^{99m}Tc-MT1-MMP mAb with decreased blood pool radioactivity within the abdominal aorta (Fig. 3d–f). Relatively high ^{99m}Tc-MT1-MMP mAb accumulations were found in the liver, spleen and kidneys of both WHHLMI and control rabbits.

Table 1 Accumulation levels of ^{99m}Tc-MT1-MMP mAb and ^{99m}Tc-IgG$_3$ in the aortic segments and major organs at 24 h after injection

Segments	^{99m}Tc-MT1-MMP mAb		^{99m}Tc-IgG$_3$
	(a) Control	(b) WHHLMI	(c) WHHLMI
Arch-ascending[a]	0.75±0.37	2.96±1.07**	2.12±0.43***
Thoracic[a]	0.40±0.12	2.48±0.72**	2.03±0.64***
Abdominal[a]	0.27±0.14	1.77±0.50**	0.97±0.51****
Total[a]	0.44±0.29	2.38±0.90**	1.65±0.76****
Blood[a]	3.76±0.89	5.86±0.93*	5.72±1.08
Vastus intermedius muscle[a]	0.23±0.15	0.48±0.64	0.23±0.22
A/B ratio	0.12±0.08	0.40±0.13**	0.30±0.14****
A/M ratio	2.50±1.9	14.3±11.6**	11.0±8.1
Liver[a]	4.23[b]	2.79[b]	ND
Spleen[a]	4.50[b]	3.52[b]	ND
Kidneys[a]	3.79[b]	3.32[b]	ND

Data are represented as the mean ± SD

A/B ratio aorta to blood ratio, *A/M ratio* aorta to muscle ratio, *ND* not determined

*$p<0.05$; **$p<0.001$ vs (a) control group; ***$p<0.05$; ****$p<0.001$ vs (b)

^{99m}Tc-MT1-MMP mAb (WHHLMI) group

[a] DUR

[b] $n=1$ due to technical problems

Accumulation levels of ^{99m}Tc-MT1-MMP mAb in the aortic segments of WHHLMI and control rabbits are summarized in Table 1. The accumulation level in each aortic segment of WHHLMI rabbits was 3.9- to 6.6-fold higher than control rabbits and the differences were significant. Mean blood pool radioactivity at 24 h was 5.86 and 3.76 (DUR) in WHHLMI and control rabbits, respectively. Aorta to blood radioactivity ratios (A/B) and aorta to muscle radioactivity ratios (A/M) were significantly higher in WHHLMI rabbits than in control rabbits. Relatively high ^{99m}Tc-MT1-MMP mAb accumulation levels were detected in the liver (4.23 in WHHLMI and 2.79 in control rabbits), spleen (4.50 in WHHLMI and 3.52 in control rabbits) and kidneys (3.79 in WHHLMI and 3.32 in control rabbits) of both rabbits. No marked difference in the distribution of ^{99m}Tc-MT1-MMP mAb in non-target

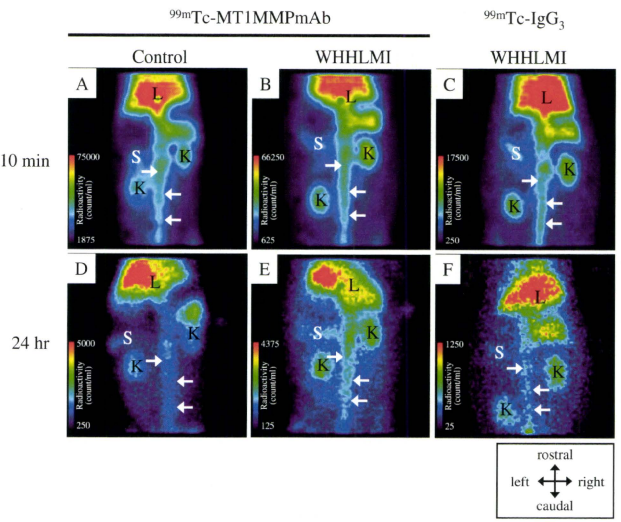

Fig. 3 Non-invasive imaging of the abdominal region with ^{99m}Tc-MT1-MMP mAb and ^{99m}Tc-IgG$_3$. Planar images for the control (**a**, **d**) and WHHLMI rabbits (**b**, **c**, **e**, **f**) at 10 min (**a**–**c**) and 24 h (**d**–**f**) after injection of ^{99m}Tc-MT1-MMP mAb (**a**, **b**, **d**, **e**) or ^{99m}Tc-IgG$_3$ (**c**, **f**). *Arrows*, *L*, *K* and *S* mark the aorta, liver, kidney and spleen, respectively

organs was observed between WHHLMI and control rabbits.

Regional distribution of ^{99m}Tc-MT1-MMP mAb in comparison with MT1-MMP expression

In the ARG study, heterogeneous ^{99m}Tc-MT1-MMP mAb accumulation was observed in the intima of WHHLMI rabbit aortas, while no marked accumulation was found in the aortas of control rabbits (Fig. 4a, b). No marked accumulation was also found in the aortas of WHHLMI rabbits given ^{99m}Tc-IgG$_3$ (Fig. 4c). MT1-MMP expression was detected in the intimal regions of the WHHLMI rabbit aorta, and the expression level was different among the regions (Fig.4e, g, h). Higher accumulation levels of ^{99m}Tc-MT1-MMP mAb were found in regions with high MT1-MMP expression, whereas lower accumulation was observed in regions with low MT1-MMP expression. No obvious MT1-MMP expression was observed in the aorta of control rabbits (Fig. 4d, f). Figure 4i, j shows the relationship of MT1-MMP expression density with ^{99m}Tc-MT1-MMP mAb accumulation and ^{99m}Tc-IgG$_3$, respectively. Regional ^{99m}Tc-MT1-MMP mAb accumulation levels in the aorta section were positively correlated with MT1-MMP expression density in WHHLMI rabbits (r=0.59, p<0.0001). On the other hand, ^{99m}Tc-IgG$_3$ accumulation was independent of MT1-MMP expression density (r=0.03, p=NS).

Relationship between ^{99m}Tc-MT1-MMP mAb accumulation and histological characteristics

Figure 2a–p shows representative photomicrographs of the histological features of each atherosclerotic lesion category in WHHLMI rabbits. The histopathological features, which correspond to the classification criteria, observed in the ascending-arch and thoracic aortas of WHHLMI rabbits were as follows: neointimal (n=15 for ^{99m}Tc-MT1-MMP mAb study and n=13 for ^{99m}Tc-IgG$_3$ study), atheromatous (n=39 and n=31, respectively), fibroatheromatous (n=36 and n=35, respectively) and collagen-rich (n=59 and n=41, respectively). No lesions showed haemorrhage, plaque rupture or thrombi (type VI) in the present study.

^{99m}Tc-MT1-MMP mAb accumulation level was dependent on the histological grade of the lesions (Fig. 5a, Table 2) and was prominently and significantly the highest (p<0.0001) in atheromatous lesions (type IV) compared with those in other lesions. Accumulation level of ^{99m}Tc-MT1-MMP mAb in atheromatous lesions was 3.3-, 2.7- and 3.0-fold higher than those in the neointimal, fibroatheromatous and collagen-rich lesions, respectively. In contrast, the ^{99m}Tc-IgG$_3$ accumulation level was markedly lower than ^{99m}Tc-MT1-MMP mAb. The ^{99m}Tc-IgG$_3$ accumulation level was independent of the histological grade of lesions, except for slightly but significantly lower ^{99m}Tc-IgG$_3$ level in the neointimal lesion (Fig. 5a, Table 2).

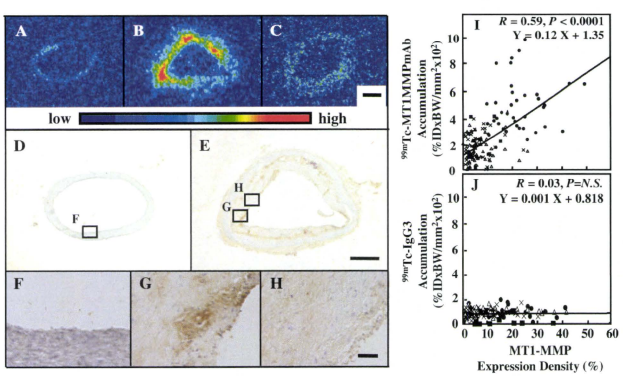

Fig. 4 Regional distribution of ^{99m}Tc-MT1-MMP mAb and ^{99m}Tc-IgG$_3$, and MT1-MMP expression in aorta sections. **a**–**c** Autoradiograms of ^{99m}Tc-MT1-MMP mAb in the control (**a**) and WHHLMI (**b**) rabbits and ^{99m}Tc-IgG$_3$ in a WHHLMI rabbit (**c**). **d**–**h** MT1-MMP immunohistochemical staining of the control (**d** and **f**) and WHHLMI rabbits (**e**, **g** and **h**). **f**–**h** High magnification images of MT1-MMP immunohistochemical staining in the regions depicted in **d** and **e**. Regression analyses of MT1-MMP expression density with ^{99m}Tc-MT1-MMP mAb accumulation (**i**) and ^{99m}Tc-IgG$_3$ (**j**) are shown. An identical colour window was applied to all autoradiographic images (**a**–**c**). *Bar* = 1 mm (**a**–**e**) and 100 μm (**f**–**h**). ■ neointimal lesion, • atheromatous lesion, x fibroatheromatous lesion, Δ collagen-rich lesion

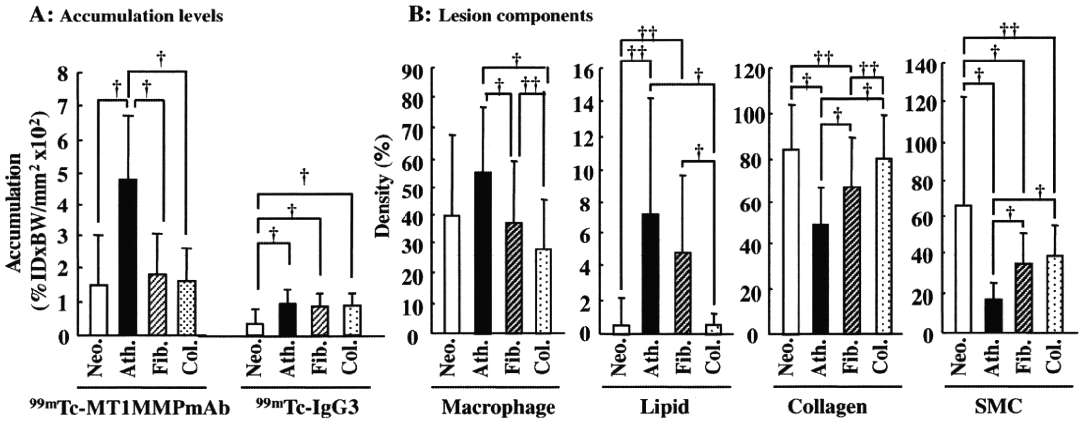

Fig. 5 Distribution profiles of ^{99m}Tc-MT1-MMP mAb, ^{99m}Tc-IgG$_3$ (**a**) and lesion components (macrophages, lipids, collagen and smooth muscle cells) (**b**) in each lesion category. *Neo.*, *Ath.*, *Fib.* and *Col.* neointimal, atheromatous, fibroatheromatous and collagen-rich lesions, respectively. *SMC* smooth muscle cells. Data are represented as the mean ± SD. †$p<0.01$; ††$p<0.05$

Figure 5b and Table 2 show the lesion components (i.e. macrophages, lipids, collagen and smooth muscle cells) quantified for each lesion category. The macrophage and lipid density was also the highest in the atheromatous lesions among the four lesion categories. Consequently, the highest level of ^{99m}Tc-MT1-MMP mAb accumulation, macrophage density and lipid density were observed in atheromatous lesions. On the other hand, the collagen and smooth muscle cell density was the lowest in atheromatous lesions among the four lesion categories.

Discussion

Aiming to develop a non-invasive means for discriminating atherosclerotic lesions at higher risk of rupture (atheromatous lesions) from more stable lesions, the potential of a radio-probe, ^{99m}Tc-MT1-MMP mAb, was evaluated in an atherosclerotic WHHLMI rabbit model. Consequently, significantly higher ^{99m}Tc-MT1-MMP mAb accumulation was found in grade IV atheroma in comparison with neointimal lesions or other more stable lesions. Thus, the potential of ^{99m}Tc-MT1-MMP mAb was demonstrated for nuclear imaging of MT1-MMP expression and selectively detecting atheromatous lesions.

Comparison with ^{99m}Tc-annexin A5 and ^{18}F-FDG

Our major interest is the prominently higher ^{99m}Tc-MT1-MMP mAb accumulation in grade IV atheroma in comparison with neointimal lesions or other more stable lesions. It will be of great importance to compare the accumulation profile of ^{99m}Tc-MT1-MMP mAb with that of ^{99m}Tc-annexin A5, a marker of ongoing apoptotic cell death, and ^{18}F-FDG, a marker of inflammation, as both ^{99m}Tc-annexin A5 and ^{18}F-FDG have been applied to clinical studies and are considered to be the most promising radio-probes for evaluation of plaque characteristics [5, 11]. Surprisingly, the accumulation

Table 2 Distribution profiles of ^{99m}Tc-MT1-MMP mAb, ^{99m}Tc-IgG$_3$ and lesion components (macrophages, lipids, collagen and smooth muscle cells) in each lesion category

	Neointimal	Atheromatous	Fibroatheromatous	Collagen-rich
^{99m}Tc-MT1-MMP mAb[a]	1.48±1.51	4.81±1.91	1.79±1.26	1.60±0.98
^{99m}Tc-IgG$_3$[a]	0.35±0.41	0.93±0.38	0.86±0.32	0.89±0.29
Macrophage[b]	39.8±27.8	55.4±21.3	37.3±22.3	27.8±17.6
Lipid[b]	1.6±2.5	7.2±7.0	4.8±4.9	0.7±0.7
Collagen[b]	84.0±18.9	48.6±18.5	66.9±22.3	80.1±18.3
SMC[b]	65.7±56.5	16.8±8.1	34.4±16.1	38.1±17.2

Data are represented as the mean ± SD. For the results of statistical analysis, see Fig. 5

[a] Accumulation (%ID×BW/mm^2 ×10^2)

[b] Density (%)

ratios of atheromatous lesions to other lesions of ^{99m}Tc-MT1-MMP mAb (**A**theromatous/**N**eointimal = 3.3, **A**theromatous/**F**ibroatheromatous = 2.7 and **A**theromatous/**C**ollagen-rich ratio = 3.0) were markedly higher than those of ^{99m}Tc-annexin A5 (**A/N**=1.3, **A/F**=1.3 and **A/C**=1.8) [28]. These results suggest the ability of ^{99m}Tc-MT1-MMP mAb to selectively detect grade IV atheroma among heterogeneous atherosclerotic lesions. On the other hand, a recent clinical study showed that vascular uptake of FDG was seen in a substantial portion (50%) of patients who had undergone FDG positron emission tomography (PET) imaging for various indications (i.e. malignant tumours, solitary pulmonary nodules or liver masses and benign diseases) [30]. Our previous study in apolipoprotein E null mice also showed relatively high ^{18}F-FDG accumulation levels in early lesions, resulting in lower accumulation ratios for advanced to early lesions in comparison with ^{99m}Tc-annexin A5 [31]. Thus, the desirable features of ^{99m}Tc-MT1-MMP mAb further confirm its potential as a radio-probe for detecting atheromatous lesions. It should be noted here that ^{18}F-FDG is considered to be the most promising probe for identifying inflamed atherosclerotic lesions. This is probably because of the higher absolute uptake levels of ^{18}F-FDG, which may be advantageous for lesion detection [28, 31, 32]. ^{18}F-FDG, as well as CT, MRI and US, can be used to find the patients whose lesion vulnerability needs to be further evaluated. The preferential uptake of ^{99m}Tc-MT1-MMP mAb in atheromatous lesions may be a useful indicator of advanced lesions, although it is still necessary to further demonstrate whether ^{99m}Tc-MT1-MMP mAb is also useful for characterizing atherosclerosis in the course of lesion development, as well as grade IV atheroma.

Immunoreactivity and specificity of ^{99m}Tc-MT1-MMP mAb

Immunoreactivity and specificity are indispensable prerequisites of in vivo nuclear imaging probes utilizing immunodetection. In this study, anti-MT1-MMP monoclonal IgG_3 (MT1-MMP mAb) was labelled with ^{99m}Tc after derivatization with HYNIC. Flow cytometry analyses indicated that modification of MT1-MMP mAb with the chelating moiety (HYNIC) does not significantly affect the immunoreactivity of the original MT1-MMP mAb. In addition, ARG and immunohistochemical studies showed that ^{99m}Tc-MT1-MMP mAb but not ^{99m}Tc-IgG_3 accumulation in atherosclerotic lesions was well correlated with MT1-MMP expression density (Fig. 4i, j). Furthermore, Fig. 5a and Table 2 confirmed the low and almost non-specific accumulation of ^{99m}Tc-IgG_3 among the lesion categories. Our previous studies also showed that accumulation of ^{99m}Tc-labelled non-specific IgG_{2a} in atheromatous lesions was not significantly different from other types of lesions (i.e. neointimal lesion, fibroatheromatous lesion, collagen-rich lesion) [33]. These findings strongly suggest the potential of ^{99m}Tc-MT1-MMP mAb to specifically recognize MT1-MMP in vivo, although experiments using radiotracers with higher radiochemical purities and further characterization of the labelled antibodies are required to confirm the present results and prove the usefulness of nuclear imaging with ^{99m}Tc-MT1-MMP mAb.

Limitations in ^{99m}Tc-MT1-MMP mAb imaging and the present study design

Another prerequisite of radio-probes is a rapid clearance of radioactivity from the blood and tissues surrounding the target lesions. One drawback of our ^{99m}Tc-MT1-MMP mAb is its relatively slow clearance from the blood, which is an intrinsic problem of radio-probes utilizing antibodies. The A/B ratio in WHHLMI rabbits was 0.40±0.13 at 24 h, indicating that the radioactivity detected in the in vivo imaging study was from both the aorta and blood. Thus, the clearance of ^{99m}Tc-MT1-MMP mAb does not match the short half-life of ^{99m}Tc. Recent advances in antibody engineering, however, should provide a promising solution to this issue. Radio-probes derived from low molecular weight polypeptides or compounds, small recombinant antibody fragments (Fab, scFv) or engineered variants (diabodies, triabodies, minibodies and single-domain antibodies) show rapid clearance of radioactivity from the circulation [34]. Pretargeting antibody methods appear to provide another solution to achieve the rapid clearance of radioactivity from the circulation [35]. Image subtraction techniques and/or kinetic model analysis, particularly those with dual isotope single photon emission computed tomography (SPECT) imaging techniques, may also help address this issue [36]. Semiconductor detector technologies contribute to separate signals from each isotope [37]. Accordingly, ^{99m}Tc-MT1-MMP mAb still appears to have the potential as an in vivo nuclear imaging probe that deserves further investigation.

Here, it should be noted that the blood level of ^{99m}Tc-MT1-MMP mAb in WHHLMI rabbits is significantly higher than that in control rabbits (Table 1). Atherosclerotic changes have been shown to be associated with hepatic and renal dysfunctions [38, 39]. Our preliminary in vitro incubation study showed that >95% of ^{99m}Tc-MT1-MMP mAb remained unchanged in rabbit plasma up to 24 h (data not shown). Accordingly, the high blood level of ^{99m}Tc-MT1-MMP mAb in WHHLMI rabbits may be caused by disturbed metabolism/excretion owing to dyshepatia or dysnephria, although the exact reason remains unclear. Our previous study on annexin A5 also showed slower blood clearance of the tracer in WHHLMI rabbits [28].

In addition to the high blood pool radioactivity, the limited spatial resolution of nuclear imaging modalities and cardiac and respiratory motion may hamper imaging of culprit lesions in moving coronary arteries. The limitation, however, may be partly solved by coregistration with CT or MRI to obtain anatomical information [11]. In this regard, PET/CT or SPECT/CT technology has gained increasing interest in the clinical imaging of atherosclerotic plaques. On the other hand, respiratory and electrocardiographic gating techniques seem to be a promising approach to solve the problem of cardiac and respiratory motion [11]. Further, SPECT imaging of small experimental animals is rapidly gaining in popularity, thanks to the development of advanced multi-pinhole collimation technologies [40]. Multi-pinhole collimation technologies may largely improve the spatial resolution of SPECT scanners, although their sensitivity is still limited. Compared with SPECT, PET has several advantages, including its higher resolution with higher sensitivity and better quantitative nature. Accordingly, the development of positron-labelled radiotracers may be another option to solve the limitation, although additional molecular design, including that for accelerating blood clearance and use of positron emitters with longer half-lives (^{64}Cu and ^{124}I), is required.

Hepatic and renal radioactivity accumulation is one of the most important concerns in nuclear imaging utilizing radiolabelled antibodies [41]. The present results showed a relatively high radioactivity accumulation in the kidneys (Table 1). It is well known that most radiolabelled mAbs show very high liver uptake due to the hepatic clearance. Unfortunately, the exact reason for the high renal accumulation remains unclear. However, it may be ascribed to the metabolic and/or degradation products of the labelled compound, as the present experiment performed at 24 h (relatively late phase) after the radiotracer injection. Low molecular weight metabolic and/or degradation products are preferentially excreted via kidneys [41]. Another explanation may be characteristics of the labelled antibody, as ^{99m}Tc-MT1-MMP mAb also showed relatively high renal accumulation in rats and mice at 1 h after the radiotracer injection [42]. Several investigators reported relatively high renal accumulation of radiolabelled mAbs [43–45]. Further studies, including in vivo metabolite analysis, would help clarify the reason for the high renal accumulation of radioactivity derived from ^{99m}Tc-MT1-MMP mAb. On the other hand, the planar images showed significantly higher radioactivity accumulation in the liver than that in the kidneys (Fig. 3). As for the discrepancy between the biodistribution and imaging studies (Table 1 and Fig. 3), the reason can be explained by the planar imaging technique used in the present study. Planar images apparently show higher radioactivity accumulation in the larger (thicker) organs, as they represent summation of radioactivity for the y-axis of the body.

MMPs as a target molecule for imaging plaques at higher risk of rupture

Macrophages secrete enzymes that degrade the fibrous cap of the plaque, including several members of MMPs [16, 46, 47]. MT1-MMP and MMP-2 expression was prominently observed in the macrophage-rich regions of the atheromatous lesions [16]. The high ^{99m}Tc-MT1-MMP mAb accumulation in grade IV atheroma found in the present study can be partly ascribed to the accumulated macrophages in the lesion as shown in Fig. 5 and Table 2. For nuclear imaging of MMPs, several broad-spectrum MMP inhibitors (MPI), including HO-CGS 27023A, have been radiolabelled [11, 12, 48]. Experimental studies in apolipoprotein E null mice indicated that ^{123}I-HO-CGS 27023A could specifically image MMP activity by scintigraphy of MMP-rich vascular lesions in vivo [49]. Another MPI, labelled with ^{111}In (RP780), has been used to image atherosclerotic lesions in a rabbit model [11, 12, 50]. A significantly higher level of immunostaining for MMPs was observed in plaque segments demonstrating higher accumulation of the ^{111}In-labelled MPI. Zhang et al. [51] also showed the potentials of ^{111}In-labelled MPI (RP782), which binds to the activated catalytic domain of MMPs, for detecting injury-induced vascular remodelling in apolipoprotein E null mice. Recently, Fujimoto et al. reported on ^{99m}Tc-labelled MPI (RP805) [52]. On the other hand, Lancelot et al. [53] demonstrated the usefulness of MMPs as a target for the characterization of atherosclerotic lesions, by using a gadolinium (Gd)-based MRI contrast agent that targets MMPs (P947, Gd-labelled MPI). These findings support the present results and indicate the potential of MMPs as a suitable target for in vivo imaging of atherosclerosis. Here, it should be noted that these radiolabelled broad-spectrum MPIs mainly recognize soluble MMPs, including MMP-2, -8, -9 and -13, while our ^{99m}Tc-MT1-MMP mAb recognizes a membrane-bound MMP, MT1-MMP (MMP-14). It may be advantageous to utilize membrane-bound MMPs as a target molecule for imaging because most soluble MMPs are released from cells, which may result in diffuse distribution of the enzymes and elevated circulating MMP levels, and may cause elevated background levels during in vivo imaging. Conversely, it remains unclear and should be clarified which MMP subtype is the most suitable target for in vivo imaging and whether specific or broad-spectrum imaging of MMPs is more useful for determining plaques at higher risk of rupture.

It is very important to discuss the potentials of target molecules other than MMPs. Our previous study in WHHLMI rabbits showed the co-distribution of MT1-

MMP, MMP-2 and cyclooxygenase 2 (COX-2) in grade IV atheroma, indicating a possible link among these enzymes in the destabilization of atherosclerotic plaques [16]. Relatively high COX-2 expression levels, however, were also observed in other more stable lesions, indicating that COX-2 is less suitable for determining plaques at higher risk of rupture. We also evaluated the potentials of lectin-like oxidized low-density lipoprotein (LDL) receptor 1 (LOX-1), a cell surface receptor for oxidized LDL, as a target molecule for determining plaques at higher risk of rupture [33]. Consequently, the accumulation ratios of ^{99m}Tc-labelled anti-LOX-1 mAb for atheromatous lesions to other lesions (**A/N** = 2.7, **A/F** = 1.9 and **A/C** lesion ratios = 2.4) were higher than those of ^{99m}Tc-annexin A5 but less than those of ^{99m}Tc-MT1-MMP mAb. These findings further confirmed the potentials of MT1-MMP as a target molecule for determining plaques at higher risk of rupture. On the other hand, several promising atherosclerosis-targeted imaging agents, including those for macrophage activity, angiogenesis, apoptosis and cell tracking, have been reported [5]. Extensive studies are now ongoing to prove which target molecule is more suitable for characterizing the vulnerability of atherosclerotic plaques and for identifying patients at higher risk of cardiovascular events [5]. Our series of studies in WHHLMI rabbits [28, 33] and apolipoprotein E null mice [31] using ^{18}F-FDG, ^{99m}Tc-annexin A5, ^{99m}Tc-labelled anti-LOX-1 [33] and ^{99m}Tc-MT1-MMP mAb successfully characterized these tracers. Further studies using these animal models should be helpful in the search for a suitable target molecule for imaging atherosclerotic plaques.

Conclusions

In this study, we succeeded in determining MT1-MMP expression in vivo utilizing a radiolabelled anti-MT1-MMP antibody and nuclear imaging techniques. Consequently, we demonstrated prominently higher accumulation of ^{99m}Tc-MT1-MMP mAb in grade IV atheroma. These findings indicate that nuclear imaging of MT1-MMP could provide new diagnostic imaging capabilities for characterizing atherosclerotic plaques, although further investigations to improve the blood clearance and target to blood ratios are strongly required.

Acknowledgments This work was partly supported by a Grant-in-Aid for General Scientific Research from the Ministry of Education, Culture, Sports, Science and Technology of Japan, and from the Japan Society for the Promotion of Science, and by a research grant from New Energy and Industrial Technology Development Organization (NEDO). This study was also partly supported by Special Coordination Funds for Promoting Science and Technology of the Ministry of Education, Culture, Sports, Science and Technology, the Japanese Government.

Conflicts of interest None.

References

1. Kolodgie FD, Virmani R, Burke AP, Farb A, Weber DK, Kutys R, et al. Pathologic assessment of the vulnerable human coronary plaque. Heart 2004;90:1385–91.
2. Lendon C, Born GV, Davies MJ, Richardson PD. Plaque fissure: the link between atherosclerosis and thrombosis. Nouv Rev Fr Hematol 1992;34:27–9.
3. Ruberg FL, Leopold JA, Loscalzo J. Atherothrombosis: plaque instability and thrombogenesis. Prog Cardiovasc Dis 2002;44:381–94.
4. Davies JR, Rudd JH, Weissberg PL. Molecular and metabolic imaging of atherosclerosis. J Nucl Med 2004;45:1898–907.
5. Jaffer FA, Libby P, Weissleder R. Molecular and cellular imaging of atherosclerosis: emerging applications. J Am Coll Cardiol 2006;47:1328–38.
6. Galis ZS, Khatri JJ. Matrix metalloproteinases in vascular remodeling and atherogenesis: the good, the bad, and the ugly. Circ Res 2002;90:251–62.
7. Galis ZS, Sukhova GK, Lark MW, Libby P. Increased expression of matrix metalloproteinases and matrix degrading activity in vulnerable regions of human atherosclerotic plaques. J Clin Invest 1994;94:2493–503.
8. Jones CB, Sane DC, Herrington DM. Matrix metalloproteinases: a review of their structure and role in acute coronary syndrome. Cardiovasc Res 2003;59:812–23.
9. Brown DL, Hibbs MS, Kearney M, Loushin C, Isner JM. Identification of 92-kD gelatinase in human coronary atherosclerotic lesions. Association of active enzyme synthesis with unstable angina. Circulation 1995;91:2125–31.
10. Li Z, Li L, Zielke HR, Cheng L, Xiao R, Crow MT, et al. Increased expression of 72-kd type IV collagenase (MMP-2) in human aortic atherosclerotic lesions. Am J Pathol 1996;148:121–8.
11. Davies JR, Rudd JH, Weissberg PL, Narula J. Radionuclide imaging for the detection of inflammation in vulnerable plaques. J Am Coll Cardiol 2006;47:C57–68.
12. Hartung D, Schäfers M, Fujimoto S, Levkau B, Narula N, Kopka K, et al. Targeting of matrix metalloproteinase activation for noninvasive detection of vulnerable atherosclerotic lesions. Eur J Nucl Med Mol Imaging 2007;34:S1–8.
13. Visse R, Nagase H. Matrix metalloproteinases and tissue inhibitors of metalloproteinases: structure, function, and biochemistry. Circ Res 2003;92:827–39.
14. Sato H, Takino T, Okada Y, Cao J, Shinagawa A, Yamamoto E, et al. A matrix metalloproteinase expressed on the surface of invasive tumour cells. Nature 1994;370:61–5.
15. Knäuper V, Bailey L, Worley JR, Soloway P, Patterson ML, Murphy G. Cellular activation of proMMP-13 by MT1-MMP depends on the C-terminal domain of MMP-13. FEBS Lett 2002;532:127–30.
16. Kuge Y, Takai N, Ishino S, Temma T, Shiomi M, Saji H. Distribution profiles of membrane type-1 matrix metalloproteinase (MT1-MMP), matrix metalloproteinase-2 (MMP-2) and cyclooxygenase-2 (COX-2) in rabbit atherosclerosis: comparison with plaque instability analysis. Biol Pharm Bull 2007;30:1634–40.
17. Rajavashisth TB, Xu XP, Jovinge S, Meisel S, Xu XO, Chai NN, et al. Membrane type 1 matrix metalloproteinase expression in human atherosclerotic plaques: evidence for activation by proinflammatory mediators. Circulation 1999;99:3103–9.
18. Stawowy P, Meyborg H, Stibenz D, Borges Pereira Stawowy N, Roser M, Thanabalasingam U, et al. Furin-like proprotein convertases are central regulators of the membrane type matrix

metalloproteinase-pro-matrix metalloproteinase-2 proteolytic cascade in atherosclerosis. Circulation 2005;111:2820–7.
19. Shiomi M, Ito T, Yamada S, Kawashima S, Fan J. Development of an animal model for spontaneous myocardial infarction (WHHLMI rabbit). Arterioscler Thromb Vasc Biol 2003;23:1239–44.
20. Abrams MJ, Juweid M, tenKate CI, Schwartz DA, Hauser MM, Gaul FE, et al. Technetium-99m-human polyclonal IgG radiolabeled via the hydrazino nicotinamide derivative for imaging focal sites of infection in rats. J Nucl Med 1990;31:2022–8.
21. Ono M, Arano Y, Mukai T, Uehara T, Fujioka Y, Ogawa K, et al. Plasma protein binding of (99m)Tc-labeled hydrazino nicotinamide derivatized polypeptides and peptides. Nucl Med Biol 2001;28:155–64.
22. Ono M, Arano Y, Uehara T, Yasushi F, Kazuma O, Namba S, et al. Intracellular metabolic fate of radioactivity after injection of technetium-99m-labeled hydrazino nicotinamide derivatized proteins. Bioconjug Chem 1999;10:386–94.
23. Larsen SK, Solomon HF, Caldwell G, Abrams MJ. [99mTc]tricine: a useful precursor complex for the radiolabeling of hydrazinonicotinate protein conjugates. Bioconjug Chem 1995;6:635–8.
24. Ishii K, Kita T, Kume N, Nagano Y, Kawai C. Uptake of acetylated LDL by peritoneal macrophages obtained from normal and Watanabe heritable hyperlipidemic rabbits, an animal model for familial hypercholesterolemia. Biochim Biophys Acta 1988;962:387–9.
25. Stary HC, Chandler AB, Dinsmore RE, Fuster V, Glagov S, Insull Jr W, et al. A definition of advanced types of atherosclerotic lesions and a histological classification of atherosclerosis. A report from the Committee on Vascular Lesions of the Council on Arteriosclerosis, American Heart Association. Circulation 1995;92:1355–74.
26. Stary HC, Chandler AB, Glagov S, Guyton JR, Insull Jr W, Rosenfeld ME, et al. A definition of initial, fatty streak, and intermediate lesions of atherosclerosis. A report from the Committee on Vascular Lesions of the Council on Arteriosclerosis, American Heart Association. Circulation 1994;89:2462–78.
27. Kobayashi S, Inoue N, Ohashi Y, Terashima M, Matsui K, Mori T, et al. Interaction of oxidative stress and inflammatory response in coronary plaque instability: important role of C-reactive protein. Arterioscler Thromb Vasc Biol 2003;23:1398–404.
28. Ishino S, Kuge Y, Takai N, Tamaki N, Strauss HW, Blankenberg FG, et al. 99mTc-Annexin A5 for noninvasive characterization of atherosclerotic lesions: imaging and histological studies in myocardial infarction-prone Watanabe heritable hyperlipidemic rabbits. Eur J Nucl Med Mol Imaging 2007;34:889–99.
29. Shiomi M, Ito T, Hirouchi Y, Enomoto M. Stability of atheromatous plaque affected by lesional composition: study of WHHL rabbits treated with statins. Ann N Y Acad Sci 2001;947:419–23.
30. Yun M, Yeh D, Araujo LI, Jang S, Newberg A, Alavi A. F-18 FDG uptake in the large arteries: a new observation. Clin Nucl Med 2001;26:314–9.
31. Zhao Y, Kuge Y, Zhao S, Morita K, Inubushi M, Strauss HW, et al. Comparison of 99mTc-annexin A5 with 18F-FDG for the detection of atherosclerosis in ApoE-/- mice. Eur J Nucl Med Mol Imaging 2007;34:1747–55.
32. Ogawa M, Ishino S, Mukai T, Asano D, Teramoto N, Watabe H, et al. (18)F-FDG accumulation in atherosclerotic plaques: immunohistochemical and PET imaging study. J Nucl Med 2004;45:1245–50.
33. Ishino S, Mukai T, Kuge Y, Kume N, Ogawa M, Takai N, et al. Targeting of lectinlike oxidized low-density lipoprotein receptor 1 (LOX-1) with 99mTc-labeled anti-LOX-1 antibody: a potential agent for imaging of vulnerable plaque. J Nucl Med 2008;49:1677–85.
34. Huhalov A, Chester KA. Engineered single chain antibody fragments for radioimmunotherapy. Q J Nucl Med Mol Imaging 2004;48:279–88.
35. Sharkey RM, Karacay H, Cardillo TM, Chang CH, McBride WJ, Rossi EA, et al. Improving the delivery of radionuclides for imaging and therapy of cancer using pretargeting methods. Clin Cancer Res 2005;11:7109s–21.
36. Watabe H, Ikoma Y, Kimura Y, Naganawa M, Shidahara M. PET kinetic analysis–compartmental model. Ann Nucl Med 2006;20:583–8.
37. Darambara DG, Todd-Pokropek A. Solid state detectors in nuclear medicine. Q J Nucl Med 2002;46:3–7.
38. Campean V, Neureiter D, Varga I, Runk F, Reiman A, Garlichs C, et al. Atherosclerosis and vascular calcification in chronic renal failure. Kidney Blood Press Res 2005;28:280–9.
39. Santoliquido A, Di Campli C, Miele L, Gabrieli ML, Forgione A, Zocco MA, et al. Hepatic steatosis and vascular disease. Eur Rev Med Pharmacol Sci 2005;9:269–71.
40. Beekman F, van der Have F. The pinhole: gateway to ultra-high-resolution three-dimensional radionuclide imaging. Eur J Nucl Med Mol Imaging 2007;34:151–61.
41. Akizawa H, Arano Y. Altering pharmacokinetics of radiolabeled antibodies by the interposition of metabolizable linkages. Metabolizable linkers and pharmacokinetics of monoclonal antibodies. Q J Nucl Med 2002;46:206–23.
42. Temma T, Sano K, Kuge Y, Kamihashi J, Takai N, Ogawa Y, et al. Development of a radiolabeled probe for detecting membrane type-1 matrix metalloproteinase on malignant tumors. Biol Pharm Bull 2009;32:1272–7.
43. Rogers BE, Anderson CJ, Connett JM, Guo LW, Edwards WB, Sherman EL, et al. Comparison of four bifunctional chelates for radiolabeling monoclonal antibodies with copper radioisotopes: biodistribution and metabolism. Bioconjug Chem 1996;7:511–22.
44. Sugimoto K, Nishimoto N, Kishimoto T, Yoshizaki K, Nishimura T. Imaging of lesions in a murine rheumatoid arthritis model with a humanized anti-interleukin-6 receptor antibody. Ann Nucl Med 2005;19:261–6.
45. D'Alessandria C, Malviya G, Viscido A, Aratari A, Maccioni F, Amato A, et al. Use of a 99mTc labeled anti-TNFalpha monoclonal antibody in Crohn's disease: in vitro and in vivo studies. Q J Nucl Med Mol Imaging 2007;51:334–42.
46. Cipollone F, Fazia M, Mezzetti A. Novel determinants of plaque instability. J Thromb Haemost 2005;3:1962–75.
47. Rudd JH, Hyafil F, Fayad ZA. Inflammation imaging in atherosclerosis. Arterioscler Thromb Vasc Biol 2009;29:1009–16.
48. Breyholz HJ, Wagner S, Levkau B, Schober O, Schäfers M, Kopka K. A 18F-radiolabeled analogue of CGS 27023A as a potential agent for assessment of matrix-metalloproteinase activity in vivo. Q J Nucl Med Mol Imaging 2007;51:24–32.
49. Schäfers M, Riemann B, Kopka K, Breyholz HJ, Wagner S, Schäfers KP, et al. Scintigraphic imaging of matrix metalloproteinase activity in the arterial wall in vivo. Circulation 2004;109: 2554–9.
50. Kolodgie F, Edwards S, Petrov A, Sachleben R, Hartung D, Weber DK. Noninvasive detection of matrix metalloproteinase upregulation in experimental atherosclerotic lesions and its abrogation by dietary modification [abstract]. Circulation 2001; 104:694.
51. Zhang J, Nie L, Razavian M, Ahmed M, Dobrucki LW, Asadi A, et al. Molecular imaging of activated matrix metalloproteinases in vascular remodeling. Circulation 2008;118:1953–60.
52. Fujimoto S, Hartung D, Ohshima S, Edwards DS, Zhou J, Yalamanchili P, et al. Molecular imaging of matrix metalloproteinase in atherosclerotic lesions: resolution with dietary modification and statin therapy. J Am Coll Cardiol 2008;52:1847–57.
53. Lancelot E, Amirbekian V, Brigger I, Raynaud JS, Ballet S, David C, et al. Evaluation of matrix metalloproteinases in atherosclerosis using a novel noninvasive imaging approach. Arterioscler Thromb Vasc Biol 2008;28:425–32.

MOLECULAR IMAGING AND BIOLOGY

Mol Imaging Biol (2010)
DOI: 10.1007/s11307-010-0418-6

RESEARCH ARTICLE

PET Imaging of Hypoxia-Inducible Factor-1-Active Tumor Cells with Pretargeted Oxygen-Dependent Degradable Streptavidin and a Novel ^{18}F-Labeled Biotin Derivative

Takashi Kudo,[1] Masashi Ueda,[1,2] Hiroaki Konishi,[1] Hidekazu Kawashima,[1,3] Yuji Kuge,[1,4] Takahiro Mukai,[5] Azusa Miyano,[1] Shotaro Tanaka,[6] Shinae Kizaka-Kondoh,[6] Masahiro Hiraoka,[6] Hideo Saji[1]

[1]*Department of Patho-Functional Bioanalysis, Graduate School of Pharmaceutical Sciences, Kyoto University, 46-29 Yoshida Shimoadachi-cho, Sakyo-ku, Kyoto 606-8501, Japan*
[2]*Radioisotopes Research Laboratory, Kyoto University Hospital, Faculty of Medicine, Kyoto University, Kyoto 606-8507, Japan*
[3]*Department of Nuclear Medicine and Diagnostic Imaging, Graduate School of Medicine, Kyoto University, Kyoto 606-8507, Japan*
[4]*Central Institute of Isotope Science, Hokkaido University, Sapporo 060-0815, Japan*
[5]*Department of Biomolecular Recognition Chemistry, Graduate School of Pharmaceutical Sciences, Kyushu University, Fukuoka 812-8582, Japan*
[6]*Department of Radiation Oncology and Image-Applied Therapy, Graduate School of Medicine, Kyoto University, Kyoto 606-8507, Japan*

Abstract

Purpose: We aimed to evaluate the feasibility of using streptavidin–biotin-based pretargeting for positron emission tomography (PET) imaging of hypoxia-inducible factor (HIF)-1-active tumors.
Procedures: We used POS, a genetically engineered form of streptavidin that selectively stabilizes in HIF-1-active cells, and (4-^{18}F-fluorobenzoyl)norbiotinamide (^{18}F-FBB), a radiolabeled biotin derivative, for performing a biodistribution study and for PET imaging. The tumoral ^{18}F-FBB accumulation was compared to the HIF-1-dependent luciferase bioluminescence and HIF-1α immunohistochemical signal.
Results: ^{18}F-FBB accumulation was observed in POS-pretargeted tumors in mice (2.85±0.55% injected dose per gram at 3 h), and clear PET images were obtained at the same time point. The tumoral ^{18}F-FBB accumulation positively correlated with luciferase bioluminescence (R=0.72, P<0.05), and most of the area showing ^{18}F-FBB accumulation corresponded to HIF-1α-positive areas.
Conclusion: Pretargeting with POS and ^{18}F-FBB is an effective approach for PET imaging of HIF-1-active areas in tumors.

Key Words: Tumor hypoxia, Hypoxia-inducible factor-1 (HIF-1), Oxygen-dependent degradation domain (ODD), Pretargeting, ^{18}F-labeled biotin derivative

Introduction

Abnormal rapid growth of tumor cells outstrips the blood supply, which develops an oxygen tension below physiologic levels (hypoxia) [1]. It appears to be strongly

Electronic supplementary material The online version of this article (doi:10.1007/s11307-010-0418-6) contains supplementary material, which is available to authorized users.

Correspondence to: Hideo Saji; *e-mail:* hsaji@pharm.kyoto-u.ac.jp

Published online: 14 September 2010

associated with malignant progression and the development of radioresistance [2, 3]. The transcription factor hypoxia-inducible factor-1 (HIF-1) has been reported to be one of the critical components of hypoxic responses [4]. Because HIF-1 was recently reported to be closely related to tumor malignancy and to hinder both chemotherapy and radiation therapy [5, 6], noninvasive imaging of HIF-1-active hypoxic tumor cells may be useful in making a qualitative diagnosis and establishing a therapy for cancer. The oxygen-sensitive alpha subunit of HIF-1 (HIF-1α) contains an oxygen-dependent degradation domain (ODD) and regulates the HIF-1 activity by inducing the degradation of HIF-1 via the ODD under normoxic conditions [7]. Therefore, it is likely that a probe that contains the ODD and induces degradation in a similar manner as HIF-1α does can be used to evaluate HIF-1 activity *in vivo*.

We have recently synthesized proteins in which the protein transduction domain (PTD) is fused to the ODD and demonstrated that these proteins were efficiently delivered to hypoxic regions and were stabilized in HIF-1-active cells [8–11]. We have also fused the PTD and the ODD with monomeric streptavidin (SAV) to produce a chimeric protein, PTD-ODD-SAV (POS), and synthesized a radiolabeled biotin derivative, (3-$^{123/125}$I-iodobenzoyl)norbiotinamide ($^{123/125}$I-IBB). POS was degraded in an oxygen-dependent manner, and a clear image of the tumor was obtained at 24 h after the injection of ^{123}I-IBB-conjugated POS. The accumulation of ^{123}I-IBB-conjugated POS in the tumor was found to correlate with the HIF-1 activity [12]. Furthermore, we were able to obtain the tumor image rapidly by using a pretargeting approach. An adequate-contrast image was obtained just 6 h after injection of ^{123}I-IBB in the pretargeting approach, while 24 h was required when using ^{123}I-IBB-conjugated POS [13].

Compared to single-photon emission computed tomography imaging, positron emission tomography (PET) imaging is more sensitive and quantitative, and provides images with a higher spatial resolution. The limited and heterogeneous expression of HIF-1 in the tumor necessitated a high-spatial-resolution device for the accurate imaging of HIF-1-expressed regions. Therefore, we attempted to obtain PET images of the HIF-1-active hypoxic tumors by using POS. Since a period of 24 h was required to obtain an adequate-contrast image by using directly radiolabeled POS [12], we adopted the pretargeting approach to reduce radiation exposure.

Fluorine-18 is one of the most widely used positron emitters because of its adequate half-life, ease of production, and low positron energy; hence, a ^{18}F-labeled biotin derivative may be useful in PET imaging. However, there have been few reports of the application of such a molecule in pretargeted imaging [14]. Therefore, we synthesized (4-^{18}F-fluorobenzoyl)norbiotinamide (^{18}F-FBB) in order to perform PET studies with POS. This study aimed to evaluate the feasibility of using POS and ^{18}F-FBB for pretargeted PET imaging of HIF-1-active areas in tumors.

Materials and Methods

Synthesis of $^{18/19}$F-FBB

N-Succinimidyl-4-fluorobenzoate (SFB, compound 2) was synthesized according to a previously described method [15]. The detailed method of FBB (compound 3) synthesis has been described in the supplemental materials (Online Resource 1).

The synthesis of ^{18}F-FBB (^{18}F-3) is outlined in Fig. 1. Fluorine-18 was produced via the ^{18}O(p,n)^{18}F nuclear reaction by using a proton beam current to irradiate ^{18}O-H_2O [16, 17]. ^{18}F-SFB (^{18}F-2) was synthesized according to a previously described method [18, 19] and obtained with decay-uncorrected radiochemical yield of 30–40%. ^{18}F-SFB was then concentrated under a stream of nitrogen and added to a solution of *N*,*N*′-dimethylformamide (DMF)/water (4:1); the DMF solution contained norbiotinamine hydrochloride (5 mg/mL). NEt_3 was added to make the solution basic. The reaction was performed at room temperature for 0.5–1 h, and the reaction mixture was loaded onto a C18 Sep-Pak cartridge (Waters, Milford, MA, USA). The C18 cartridge was eluted with water and then with acetonitrile. The acetonitrile fraction was evaporated, and the residue was purified using high performance liquid chromatography (HPLC) (Cosmosil 5C_{18}MS-II column; Nacalai Tesque, Kyoto, Japan; 25% acetonitrile; flow rate, 1 mL/min). The retention time of ^{18}F-FBB was 11 min. The radiochemical purity was measured using HPLC, and the specific activity was determined on the basis of the ultraviolet absorbance at 254 nm. The solvent was removed by rotary evaporation and reconstituted in water or saline for use in *in vitro* and *in vivo* studies.

Preparation of Fusion Protein

POS was overexpressed in *Escherichia coli* and purified as described in a previous report [12]. Purified POS was dissolved in Tris–HCl buffer (pH 8.0).

Binding of POS and ^{18}F-FBB

^{18}F-FBB, D-biotin (0–500 pmol), and POS (0.04 pmol) were mixed and incubated in 100 mM citrate buffer (pH 5.0) for 1 h at 37°C. The binding of ^{18}F-FBB to POS in the absence of D-biotin was detected using size-exclusion chromatography (PD-10; GE Healthcare Bioscience, Uppsala, Sweden). The reaction mixture containing D-biotin was applied to an Amicon Microcon filter (Millipore) and centrifuged at 4,500×*g* for 30 min at 4°C (Micro Cooling Centrifuge 1720; Kubota, Osaka, Japan). The radioactivities of the reactant and filtrate (unbound ^{18}F-FBB) were measured, and the binding rate was calculated. All measurements were performed in triplicate.

Cell and Cell Culture

FM3A mouse mammary tumor cells were purchased from Health Science Research Resources Bank (Osaka, Japan). Suit2 human pancreatic tumor cells were originally obtained from the American Type Culture Collection (Manassas, VA, USA). Suit2/5HRE-

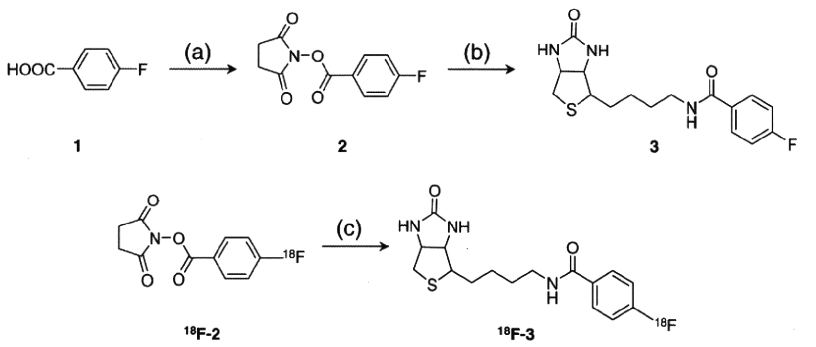

Fig. 1. Synthesis of FBB (3) and ^{18}F-FBB (^{18}F-3). (a) *N,N,N',N'*-Tetramethyl-*O*-(*N*-succinimidyl)uranium tetrafluoroborate, CH_3CN, 90°C, 10 h. (b) Norbiotinamine, NEt_3, DMF/H_2O (4:1), r.t., 5 h. (c) Norbiotinamine, NEt_3, DMF/H_2O (4:1), r.t., 1 h.

CMV_{mp}-Luciferase (Suit2/Luc) cells that express luciferase in response to HIF-1 activity were established and supplied by Prof. Kizaka-Kondoh [20]. Both cell types were cultured using a previously reported method [12, 13].

Animal Model

Animal studies were conducted in accordance with our institutional guidelines, and the experimental procedures were approved by the Kyoto University Animal Care Committee. Female C3H/He mice and BALB/c *nu/nu* mice at 5 weeks of age were purchased from Japan SLC, Inc. (Hamamatsu, Japan). Models of FM3A and Suit2/Luc tumors were prepared as described in a previous report [12]. After tumor implantation, mice were fed an AIN76-A-based, biotin-free diet (Oriental Yeast Co. Ltd., Tokyo, Japan) in order to prevent dietary biotin from inhibiting the binding of ^{18}F-FBB to POS. The mice were subjected to a tracer study at 2–3 weeks after the implantation. The average diameter and average volume of the tumors were approximately 10 mm and 500 mm^3, respectively.

Biodistribution

^{18}F-FBB (370 kBq) was injected intravenously into FM3A-implanted mice (n=4–5); the mice were sacrificed at 0.5, 1, 3, and 6 h after the injection. For the pretargeting study, we used the protocol that has been previously reported as an optimal method [13]. The mice (n=4–5) were intravenously injected with 30 μg of POS; after 24 h, ^{18}F-FBB (370 kBq) was injected intravenously. The mice were sacrificed at the same time points as mentioned above. Whole organs were immediately obtained and weighed, and their radioactivity was measured. The results were expressed in terms of the percent injected dose per gram of tissue (%ID/g).

In Vivo Blocking Study

FM3A-implanted mice (n=4) were pretargeted with POS (30 μg); after 23.5 h, the mice were injected with a vehicle or saline solution of D-biotin (1 nmol). After another 30 min, ^{18}F-FBB (370 kBq) was administered and 3 h later, the mice were sacrificed. Whole organs were immediately removed and weighed, and their radioactivity was measured. The results were expressed as %ID/g.

^{18}F-FBB Accumulation vs. HIF-1 Transcriptional Activity in Tumors in Mice Pretargeted with POS

Some Suit2/Luc-implanted mice (n=8) were pretargeted with 30 μg of POS. After 24 h, ^{18}F-FBB (370 kBq for five mice and 18.5 MBq for three mice) was administered intravenously. For immunohistochemical analysis, the mice that received the higher dose of ^{18}F-FBB were intraperitoneally injected with pimonidazole (PIMO, 60 mg/kg) 1 h after the ^{18}F-FBB injection. Further, 2.5 h after the ^{18}F-FBB injection, 200 μL of D-luciferin solution (10 mg/mL in PBS; VivoGlo Luciferin, Promega, WI, USA) was injected intraperitoneally. After 20 min, the mice were anesthetized with 2.5% isoflurane, and bioluminescence imaging was performed using IVIS Spectrum System (Xenogen, Alameda, CA, USA). The signal intensity within the tumors was analyzed using Living Image 3.0 software (Xenogen). The mice were sacrificed 3 h after the ^{18}F-FBB injection, the radioactivity of the tumors was measured, and the results were expressed in terms of %ID. The tumor specimens obtained from the mice injected with the higher dose of ^{18}F-FBB were subjected to an autoradiographic study.

Another set of Suit2/Luc-implanted mice (n=4) were pretargeted with 30 μg of POS. After 24 h, ^{18}F-FBB (18.5 MBq) was administered intravenously and 6 h later, the bioluminescence signal and radioactivity were compared using the procedure described above. After the radioactivity measurement, the tumor specimens were subjected to metabolite analysis.

Size-Exclusion Analysis of Radioactive Compounds in Tumors

After bioluminescence imaging, each mouse was anesthetized with 2.5% isoflurane, and urine was collected from its bladder. The mice were then sacrificed, and their tumors were immediately removed. Extracts were prepared using a previously reported method [13], with a slight modification. In brief, the tumors were homogenized in ice-cold 0.1 M Tris–HCl buffer containing 1% sodium dodecyl sulfate and 0.15 M NaCl (pH 6.5), by using a Polytron homogenizer (PT10-35; Kinematica AG, Switzerland). The preparations were then centrifuged at 4°C and 4,600×g for 20 min. The

supernatants and urine were analyzed by size-exclusion chromatography with a PD-10 column.

Autoradiography

Autoradiographic studies were performed on the same mice used for the bioluminescence imaging (n=3). Ten-micrometer-thick frozen tumor sections were prepared according to a previously reported procedure [21]. The sections were exposed to imaging plates (BAS-SR; Fuji Photo Film Co., Ltd., Tokyo, Japan) for 3 h, and autoradiograms were then obtained and analyzed as previously described [21], except that BAS5000 was used instead of BAS3000 (both scanners, Fuji Photo Film Co., Ltd.).

Immunohistochemical Analysis

The adjacent 10-μm-thick sections used in the autoradiographic study were subjected to dual fluorescent immunostaining for HIF-1α and PIMO according to a previously described method [13]. In brief, the sections were fixed, blocked, and treated with anti-human/mouse HIF-1α polyclonal antibody (R&D Systems, Minneapolis, MN, USA), as a primary antibody. The specific signals were detected using an Alexa Fluor 568-conjugated $F(ab')_2$ fragment of goat anti-rabbit antibody (Invitrogen, San Diego, CA, USA). Thereafter, the sections were washed with PBS and treated with fluorescein isothiocyanate-conjugated mouse IgG_1 monoclonal antibody (Chemicon, Temecula, CA, USA) according to the manufacturer's protocol for PIMO staining. The sections were then dried and coverslipped using an antifade reagent (ProLong Gold with DAPI; Invitrogen). Another adjacent section was stained with hematoxylin–eosin (HE). Fluorescent and bright-field microscopic images were obtained using BIOREVO BZ-9000 (Keyence Corp., Osaka, Japan).

PET Imaging

^{18}F-FBB (22.2±6.7 MBq) was injected into the tail veins of FM3A-implanted mice (n=6) 24 h after they were pretargeted with POS (30 μg). The mice were anesthetized with 2.5% isoflurane and placed on a scanner bed in the prone position. At 3 h after the injection, the mice were imaged for 15 min by using eXplore VISTA (GE Healthcare Bioscience). An energy window of 250–700 keV was used. Before reconstruction, the raw data were corrected for random and scattered coincidences, and radioactive decay. Attenuation correction was not performed. PET images were reconstructed according to a standard filtered back-projection procedure (FBP) with a Ramp filter (alpha, 1.0; cutoff, 1.0) or by using a two-dimensional ordered-subset expectation maximization algorithm (2D-OSEM; iterations, 2; subsets, 16). The regions of interest were drawn on the tumor and the corresponding area in the left thigh of the FBP-reconstructed images.

Statistical Analyses

The two groups were compared using the Mann–Whitney U test, and correlation coefficients were assessed using the Spearman rank analysis. Values of $P<0.05$ were considered statistically significant.

Results

Radiosynthesis of ^{18}F-FBB

The decay-uncorrected radiochemical yield from ^{18}F-SFB as a starting material was 38%; radiochemical purity, >95%; total synthesis time, 70–100 min; and specific activity at the end of synthesis, >97 GBq/μmol (limit of detection).

Binding of POS and ^{18}F-FBB

After the incubation of ^{18}F-FBB with POS, the radioactivity was detected at macromolecular fraction, as determined using size-exclusion chromatography; this indicated that ^{18}F-FBB bound to POS (data not shown). The binding of ^{18}F-FBB to POS was not inhibited by D-biotin at concentrations <100 nM (binding rate, 99.7±0.2%), whereas it was completely inhibited by 1,000 nM D-biotin (binding rate, 6.0±1.3%); the results of inhibition study are similar to those using ^{18}F-FBB alone (5.5±0.5%), *i.e.*, in the case of non-specific absorption to the column (Fig. 2).

Biodistribution

An examination of the biodistribution of ^{18}F-FBB alone revealed that both the tumor-to-blood and the tumor-to-

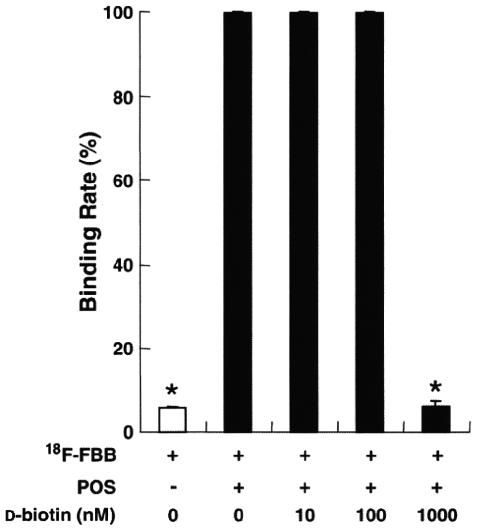

Fig. 2. Binding of ^{18}F-FBB to POS. The *black columns* represent the mean calculated binding rate of ^{18}F-FBB and POS in the presence of various concentrations of D-biotin. The *white column* represents the calculated binding rate of ^{18}F-FBB alone, which indicates non-specific absorption to the column. D-biotin (1,000 nM) significantly inhibited ^{18}F-FBB binding to POS compared to the binding in the other D-biotin-treated group (*$P<0.05$).

Table 1. Biodistribution of ^{18}F-FBB in FM3A-implanted mice

Organ	Time after injection (h)			
	0.5	1	3	6
Blood	1.68±0.19	0.86±0.12	0.10±0.07	0.04±0.01
Liver	12.07±1.11	7.30±1.24	0.44±0.06	0.24±0.11
Kidney	10.19±1.14	6.42±0.75	0.42±0.07	0.24±0.12
Intestine	17.99±1.92	21.12±7.27	7.72±1.15	3.72±1.81
Tumor	1.38±0.60	0.77±0.29	0.11±0.10	0.05±0.03
Muscle	2.08±0.23	1.70±0.74	0.09±0.06	0.13±0.08
Bone	1.14±0.96	1.54±0.52	0.27±0.20	0.20±0.17
Tumor/blood	0.83±0.39	0.90±0.30	0.64±0.20	0.94±0.30
Tumor/muscle	0.66±0.26	0.66±0.71	0.95±0.61	0.36±0.37

Organ uptake values are expressed as the percent injected dose per gram of tissue, except in the case of the tumor/blood and tumor/muscle ratios. Values are represented as the mean±SD. n=4–5

muscle ratios were less than 1 at all time points. This indicated that ^{18}F-FBB did not accumulate in the tumors. Moreover, ^{18}F-FBB was rapidly cleared from all organs, except the intestine (Table 1). In contrast, in the pretargeted group, tumor accumulation of ^{18}F-FBB 3 h after injection was 2.85±0.55% ID/g, which was more than 20-fold than for ^{18}F-FBB alone (0.11±0.10% ID/g) (Table 2). The tumor-to-blood and tumor-to-muscle ratios were greater than 1 as early as 30 min after the injection, and both these ratios increased in a time-dependent manner because of the rapid clearance of ^{18}F-FBB from the body. Although ^{18}F-FBB accumulation in the kidneys and intestine was high, the radioactivity in the other normal tissues showed a more rapid decrease than in the tumor (Table 2). Pretreatment with D-biotin markedly decreased ^{18}F-FBB accumulation (80%) in the tumors (Table 3). The ^{18}F-FBB accumulation in the other tissues also decreased following treatment with D-biotin.

^{18}F-FBB Accumulation vs. HIF-1 Transcriptional Activity in Tumors in Mice Pretargeted with POS

A significant positive correlation was observed between HIF-1-induced luciferase bioluminescence and ^{18}F-FBB accumulation 3 h after injection in tumors in mice pretargeted with POS (R=0.72, P<0.05; Fig. 3). A similar correlation was also observed at 6 h after the injection (R=0.70, P<0.05, data not shown).

Table 2. Biodistribution of ^{18}F-FBB in FM3A-implanted mice pretargeted with POS

Organ	Time after injection (h)			
	0.5	1	3	6
Blood	2.79±0.57	1.54±0.47	0.56±0.16	0.57±0.22
Liver	15.02±2.05	12.69±1.86	5.74±1.18	3.76±0.51
Kidney	21.59±3.24	19.52±2.71	9.22±1.92	4.87±0.99
Intestine	12.68±2.60	13.68±2.52	5.95±1.57	1.64±0.51
Tumor	4.65±0.49	4.70±0.97	2.85±0.55	2.48±0.49
Muscle	2.49±0.71	2.55±1.21	0.93±0.40	0.29±0.15
Bone	2.82±0.26	3.92±2.42	1.27±0.42	0.91±0.22
Tumor/blood	1.73±0.47	3.16±0.59	5.36±1.32	4.91±2.04
Tumor/muscle	1.98±0.54	2.18±0.75	3.93±2.50	9.51±3.31

Organ uptake values are expressed as the percent injected dose per gram of tissue, except in the case of the tumor/blood and tumor/muscle ratios. Values are represented as the mean±SD. n=4–5

Table 3. Blocking study of the biodistribution of ^{18}F-FBB in FM3A-implanted mice pretargeted with POS

Organ	Vehicle	D-biotin pretreatment
Blood	0.66±0.06	0.22±0.10*
Liver	3.58±1.00	1.48±0.67*
Kidney	3.39±1.05	0.80±0.41*
Intestine	6.59±2.76	7.90±0.98
Tumor	2.06±0.29	0.34±0.14*
Muscle	0.28±0.04	0.14±0.06*
Bone	1.50±1.37	1.31±0.38
Tumor/blood	4.00±2.38	1.63±0.19*
Tumor/muscle	7.29±0.94	2.53±1.19**

Organ uptake values are expressed as the percent injected dose per gram of tissue, except in the case of the tumor/blood and tumor/muscle ratios. Values are represented as the mean±SD. n=4
*P<0.05, **P<0.01 vs. vehicle group

Size-Exclusion Analysis of Radioactive Compounds in Tumors

The recovery of radioactivity from the tumor samples was 94±7.4%, and that from the PD-10 columns was 98±14%. A major proportion of the radioactivity was eluted in a macromolecular fraction (79±5.8%, n=4).

Urine analysis was performed using two samples because the quantity of urine obtained from two mice was too small. In the case of the urine samples, the recovery of radioactivity from the PD-10 columns was 92% and 99%. More than 99% of the radioactivity of both samples was eluted in a small-molecule fraction.

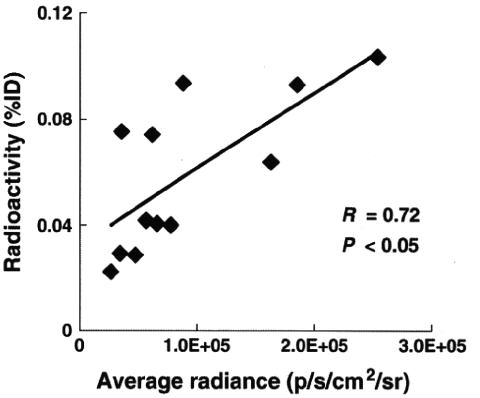

Fig. 3. Correlation between the ^{18}F-FBB accumulation at 3 h post-injection and HIF-1 activity within a tumor pretargeted with POS. The ordinate represents accumulated radioactivity (%ID), and the abscissa represents HIF-1-induced luciferase bioluminescence. The correlation coefficient (R) was 0.72, indicating a highly significant correlation (P<0.05).

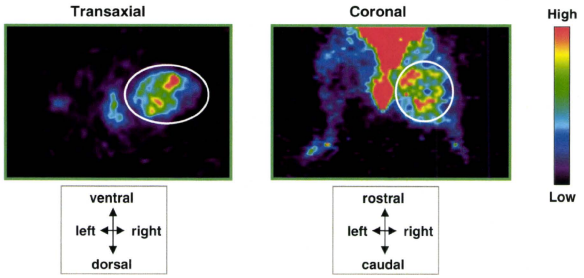

Fig. 4. Typical PET images of FM3A-implanted mice. The mice were pretargeted with POS, and 24 h later, they were intravenously injected with ^{18}F-FBB. Images were acquired 3 h after the ^{18}F-FBB injection and reconstructed using 2D-OSEM. Tumors can be clearly visualized in both images (*circle*).

PET Imaging

The high-resolution PET imaging of the mice clearly showed the tumors implanted in the right thigh (Fig. 4). The calculated tumor-to-muscle ratio was 3.4±1.4.

Histology, Autoradiography, and Immunohistochemistry

HE staining revealed the presence of necrotic areas in the tumor (Fig. 5a). PIMO-positive areas were located in the center of the section, surrounding the necrotic core (Fig. 5b), whereas HIF-1α-positive areas were present peripherally (Fig. 5c). The autoradiogram showed that the distribution of ^{18}F-FBB in the POS-pretargeted tumor was heterogeneous (Fig. 5d). Most of the ^{18}F-FBB-accumulated areas corresponded to the HIF-1α-positive areas. These findings were similar for each tumor examined in this study.

Discussion

The most important aspect of the present study was to evaluate whether the accumulation of ^{18}F-FBB in POS-pretargeted tumors reflects the level of HIF-1 expression or activity. For this purpose, we compared ^{18}F-FBB accumulation with HIF-1 transcriptional activity and HIF-1 immunohistochemical signal among tumors in the same animals that expressed the HIF-1-dependent luciferase reporter gene. In the tumors in the mice pretargeted with POS, the accumulated radioactivity at both 3 and 6 h after the administration of ^{18}F-FBB significantly correlated with the luciferase bioluminescence, *i.e.*, the HIF-1 activity. Furthermore, the tumor-to-blood ratios at 3 and 6 h were also similar. On the basis of these results, we performed the PET-imaging study at 3 h after the injection of ^{18}F-FBB because imaging in the early phase after probe injection is preferred in order to avoid radioactive decay and to reduce radiation exposure. The PET images showed the heterogeneous intratumoral distribution of ^{18}F-FBB in the mice pretargeted

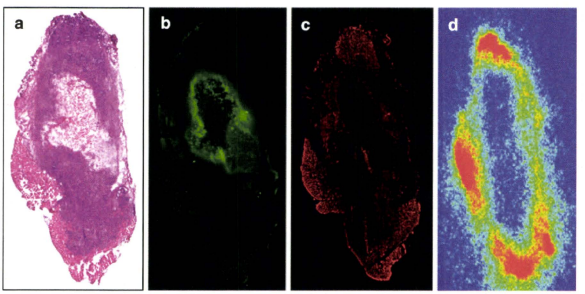

Fig. 5. Representative images of HE staining (**a**), PIMO immunostaining (**b**), HIF-1α immunostaining (**c**), and autoradiography (**d**).

with POS; this result would reflect the HIF-1-active regions because the intratumoral HIF-1-active regions have been reported to be heterogeneous [22]. In fact, the majority of ^{18}F-FBB-accumulated areas corresponded to the HIF-1α-positive areas observed on autoradiography. Therefore, these findings indicate that PET imaging with POS pretargeting and the use of ^{18}F-FBB can help detect intratumoral HIF-1-active regions. These findings are in accordance with those of our previous study where ^{123}I-IBB was used instead of ^{18}F-FBB [13]. Because the lipophilicity of ^{18}F-FBB is lower than that of ^{123}I-IBB, ^{18}F-FBB showed faster blood clearance and a higher tumor-to-blood ratio within a short duration after the injection.

Some hypoxia-imaging probes—such as ^{18}F-fluoromisonidazole (^{18}F-FMISO), 1-α-D-(5-deoxy-5-^{18}F-fluoroarabinofuranosyl)-2-nitroimidazole (^{18}F-FAZA), and ^{64}Cu-diacetyl-bis(N^4-methylthiosemicarbazone) (^{64}Cu-ATSM)—have been developed [23, 24]. These probes can detect low oxygen pressures (less than 10 mmHg) and are useful in predicting the efficacy of radiotherapy [25]. In the present study, the distribution pattern of ^{18}F-FBB in the POS-pretargeted tumor was different from that in the PIMO-positive areas. This result is somewhat different from that obtained in our previous studies where ^{125}I-IBB, which was used in the pretargeting study, and ^{125}I-IPOS were mainly distributed near the PIMO-positive areas [12, 13]. One reason for this discordant result may be the difference in the tumor models used. Suit2 pancreatic tumor cells were used for the autoradiographic and histological analyses in the present study, whereas MDA-MB-231 mammary tumor cells were used in the case of the ^{125}I-IPOS study [12]. Another reason could be the difference in tumor size. The tumor volume used in the present study was approximately 1.5 times greater than that used in the ^{125}I-IBB study [13]. In fact, even with the same tumor model, similarity between the distribution patterns of HIF-1α- and PIMO-positive areas depended on the tumor size; these areas were adjacently located in small tumors but had a different distribution pattern in large tumors [26]. Oh *et al.* reported that ^{64}Cu-ATSM accumulated on the surface of the tumor, whereas PIMO-positive areas located in the center [27]. This finding is similar to that obtained in the present study on ^{18}F-FBB distribution patterns in POS-pretargeted tumors; however, the researchers have not determined HIF-1α expression in the tumor model used in their study. A direct comparison between the POS/^{18}F-FBB system and other hypoxia-imaging probes will help to clarify the differences in the characteristics of the tumor cells that existed in each area where probe accumulation was observed, and in the information obtained from each image.

The basic requirements of an effective biotin derivative for the pretargeting approach include stability against metabolism *in vivo*, rapid clearance from the circulation, and a binding affinity to (strept)avidin. The first-generation radiolabeled biotin derivatives were easily degraded by biotinidase [28]. Biotinidase-mediated degradation can be stopped by creating a reversed amide bond (*i.e.*, NH–CO bond) between the valeryl chain of biotin and the prosthetic group [29]. On the basis of these reports, we decided to convert the terminal carboxylic group of biotin into a primary amine. We found that ^{18}F-FBB stably existed in mouse plasma (data shown in the supplemental materials, Online Resource 2), indicating that this compound was resistant to degradation by biotinidase. The results of the biodistribution study revealed that the accumulated radioactivity in the bone was low and that it did not increase in a time-dependent manner. These results suggest that ^{18}F-FBB is resistant to defluorination *in vivo*. Furthermore, ^{18}F-FBB was rapidly cleared from the blood. ^{18}F-FBB bound to POS and the binding was inhibited by D-biotin both *in vitro* and *in vivo*. These results indicate that ^{18}F-FBB meets the basic requirements of an effective biotin derivative for use in the pretargeting approach.

We found that ^{18}F-FBB accumulated in the POS-pretargeted tumors. Further, this accumulation was inhibited by D-biotin, and a major proportion of the radioactivity of the tumor was attributable to macromolecules. Taken together, these results indicate that the intratumoral radioactivity was caused by the binding of ^{18}F-FBB to the SAV moiety of POS. Thus, we concluded that ^{18}F-FBB can bind streptavidin not only *in vitro* but also *in vivo*. The amount of ^{18}F-FBB accumulation in the tumor was not as high as that of ^{18}F-FDG [30]; this finding could have been due to the limited expression of HIF-1. The expression of HIF-1 is not ubiquitous, but heterogeneous, and is small in tumors [31]. In fact, radioligand accumulation in tumors harboring HIF-1-dependent reporter genes has been reported to range from 1% to 2% ID/g in previous studies [31–33]. Furthermore, the amount of ^{18}F-FBB accumulation was similar to that of other hypoxia-imaging probes such as ^{18}F-FMISO and ^{64}Cu-ATSM (2–5% ID/g) [30, 34, 35].

In the pretargeted group, some abdominal organs showed higher radioactivity accumulation than the tumor. The high background activity in the abdominal region hampers the evaluation of the HIF-1 activity in the abdomen and pelvis, and further modification is required for such an evaluation. The radioactivity of the liver and kidneys may be attributable to the high accumulation of POS in these tissues [12]. Pretreatment of D-biotin decreased ^{18}F-FBB accumulation in the liver and kidneys, suggesting that not all the POS in these tissues was degraded or cleared within 24 h. The slow rate of degradation is a drawback of using POS. Optimization of the interval between the POS and ^{18}F-FBB administration is necessary when imaging HIF-1-active regions in the liver and kidneys. On the other hand, the radioactivity in the intestine was not blocked by D-biotin pretreatment. It is reported that biotinidase, which is involved in the transport of biotin, exists in the intestine [36]. Thus, radioactivity accumulation in the intestine would reflect the behavior of ^{18}F-FBB itself, and not its binding to POS. In this case, the biotin derivatives that show faster clearance from the body [37] may be effective agents.

Conclusion

We have developed a novel radiolabeled biotin derivative, ^{18}F-FBB, and confirmed its ability to bind to the streptavidin moiety both *in vitro* and *in vivo*. ^{18}F-FBB accumulated in the tumors pretargeted with POS; these tumors were clearly visualized on PET imaging. The accumulation of ^{18}F-FBB significantly correlated with the HIF-1 transcriptional activity, and the intratumoral distribution of ^{18}F-FBB corresponded to HIF-1α-positive areas in the tumors pretargeted with POS. These findings suggest that POS and ^{18}F-FBB are potent probes for the PET imaging of HIF-1-active areas in tumors.

Acknowledgments. We are grateful to Hiroyuki Kimura, Kenji Tomatsu, and Yu Ogawa for preparation of ^{18}F-SFB, and Kei Ogawa for skilled technical assistance.

This study was supported in part by Health Labour Sciences Research Grant for Research on Advanced Medical Technology from the Ministry of Health, Labour and Welfare of Japan; "R&D of Molecular Imaging Equipment for Malignant Tumor Therapy Support" by the New Energy and Industrial Technology Development Organization (NEDO), Japan; and a Grant-in-Aid for Exploratory Research (17659010) and a Grant-in-Aid for Young Scientists (B) (21791187) from the Ministry of Education, Culture, Sports, Science and Technology of Japan.

Conflict of interest. The authors have no conflict of interest.

References

1. Vaupel P, Kallinowski F, Okunieff P (1989) Blood flow, oxygen and nutrient supply, and metabolic microenvironment of human tumors: a review. Cancer Res 49:6449–6465
2. Brown JM (2000) Exploiting the hypoxic cancer cell: mechanisms and therapeutic strategies. Mol Med Today 6:157–162
3. Hockel M, Vaupel P (2001) Tumor hypoxia: definitions and current clinical, biologic, and molecular aspects. J Natl Cancer Inst 93:266–276
4. Semenza GL (2007) Life with oxygen. Science 318:62–64
5. Semenza GL (2003) Targeting HIF-1 for cancer therapy. Nat Rev Cancer 3:721–732
6. Dewhirst MW, Cao Y, Moeller B (2008) Cycling hypoxia and free radicals regulate angiogenesis and radiotherapy response. Nat Rev Cancer 8:425–437
7. Wang GL, Jiang BH, Rue EA, Semenza GL (1995) Hypoxia-inducible factor 1 is a basic-helix-loop-helix-PAS heterodimer regulated by cellular O_2 tension. Proc Natl Acad Sci U S A 92:5510–5514
8. Harada H, Kizaka-Kondoh S, Li G et al (2007) Significance of HIF-1-active cells in angiogenesis and radioresistance. Oncogene 26:7508–7516
9. Harada H, Kizaka-Kondoh S, Hiraoka M (2005) Optical imaging of tumor hypoxia and evaluation of efficacy of a hypoxia-targeting drug in living animals. Mol Imaging 4:182–193
10. Kizaka-Kondoh S, Konse-Nagasawa H (2009) Significance of nitroimidazole compounds and hypoxia-inducible factor-1 for imaging tumor hypoxia. Cancer Sci 100:1366–1373
11. Kizaka-Kondoh S, Tanaka S, Harada H, Hiraoka M (2009) The HIF-1-active microenvironment: an environmental target for cancer therapy. Adv Drug Deliv Rev 61:623–632
12. Kudo T, Ueda M, Kuge Y et al (2009) Imaging of HIF-1-active tumor hypoxia using a protein effectively delivered to and specifically stabilized in HIF-1-active tumor cells. J Nucl Med 50:942–949
13. Ueda M, Kudo T, Kuge Y et al (2010) Rapid detection of hypoxia-inducible factor-1-active tumours: pretargeted imaging with a protein degrading in a mechanism similar to hypoxia-inducible factor-1α. Eur J Nucl Med Mol Imaging 37:1566–1574
14. Shoup TM, Fischman AJ, Jaywook S, Babich JW, Strauss HW, Elmaleh DR (1994) Synthesis of fluorine-18-labeled biotin derivatives: biodistribution and infection localization. J Nucl Med 35:1685–1690
15. Vaidyanathan G, Zalutsky MR (2006) Synthesis of N-succinimidyl 4-[^{18}F]fluorobenzoate, an agent for labeling proteins and peptides with ^{18}F. Nat Protoc 1:1655–1661
16. Hara T, Higashi T, Nakamoto Y et al (2009) Significance of chronic marked hyperglycemia on FDG-PET: is it really problematic for clinical oncologic imaging? Ann Nucl Med 23:657–669
17. Ono M, Watanabe R, Kawashima H et al (2009) Fluoro-pegylated chalcones as positron emission tomography probes for *in vivo* imaging of beta-amyloid plaques in Alzheimer's disease. J Med Chem 52:6394–6401
18. Kimura H, Tomatsu K, Kawashima H et al (2009) Development of one-flow synthesis method for N-succinimidyl 4-[F-18]fluorobenzoate ([F-18]SFB) using microreactor for 3-step-reaction. J Label Compd Radiopharm 52:S9–S9
19. Tang G, Zeng WB, Yu MX, Kabalka G (2008) Facile synthesis of N-succinimidyl 4-[F-18]fluorobenzoate ([F-18]SFB) for protein labeling. J Label Compd Radiopharm 51:68–71
20. Kizaka-Kondoh S, Itasaka S, Zeng L et al (2009) Selective killing of hypoxia-inducible factor-1-active cells improves survival in a mouse model of invasive and metastatic pancreatic cancer. Clin Cancer Res 15:3433–3441
21. Ueda M, Iida Y, Tominaga A et al (2010) Nicotinic acetylcholine receptors expressed in the ventralposterolateral thalamic nucleus play an important role in anti-allodynic effects. Br J Pharmacol 159:1201–1210
22. Picchio M, Beck R, Haubner R et al (2008) Intratumoral spatial distribution of hypoxia and angiogenesis assessed by ^{18}F-FAZA and ^{125}I-Gluco-RGD autoradiography. J Nucl Med 49:597–605
23. Krohn KA, Link JM, Mason RP (2008) Molecular imaging of hypoxia. J Nucl Med 49 Suppl 2:129S–148S
24. Mees G, Dierckx R, Vangestel C, Van de Wiele C (2009) Molecular imaging of hypoxia with radiolabelled agents. Eur J Nucl Med Mol Imaging 36:1674–1686
25. Dunphy MP, Lewis JS (2009) Radiopharmaceuticals in preclinical and clinical development for monitoring of therapy with PET. J Nucl Med 50 Suppl 1:106S–121S
26. Lehmann S, Stiehl DP, Honer M et al (2009) Longitudinal and multimodal *in vivo* imaging of tumor hypoxia and its downstream molecular events. Proc Natl Acad Sci U S A 106:14004–14009
27. Oh M, Tanaka T, Kobayashi M et al (2009) Radio-copper-labeled Cu-ATSM: an indicator of quiescent but clonogenic cells under mild hypoxia in a Lewis lung carcinoma model. Nucl Med Biol 36:419–426
28. Chauhan J, Dakshinamurti K (1986) Purification and characterization of human serum biotinidase. J Biol Chem 261:4268–4275
29. Foulon CF, Alston KL, Zalutsky MR (1997) Synthesis and preliminary biological evaluation of (3-iodobenzoyl)norbiotinamide and ((5-iodo-3-pyridinyl)carbonyl)norbiotinamide: two radioiodinated biotin conjugates with improved stability. Bioconjug Chem 8:179–186
30. Liu RS, Chou TK, Chang CH et al (2009) Biodistribution, pharmacokinetics and PET imaging of [^{18}F]FMISO, [^{18}F]FDG and [^{18}F]FAc in a sarcoma- and inflammation-bearing mouse model. Nucl Med Biol 36:305–312
31. Serganova I, Doubrovin M, Vider J et al (2004) Molecular imaging of temporal dynamics and spatial heterogeneity of hypoxia-inducible factor-1 signal transduction activity in tumors in living mice. Cancer Res 64:6101–6108
32. Hsieh CH, Kuo JW, Lee YJ, Chang CW, Gelovani JG, Liu RS (2009) Construction of mutant TKGFP for real-time imaging of temporal dynamics of HIF-1 signal transduction activity mediated by hypoxia and reoxygenation in tumors in living mice. J Nucl Med 50:2049–2057
33. Wen B, Burgman P, Zanzonico P et al (2004) A preclinical model for noninvasive imaging of hypoxia-induced gene expression; comparison with an exogenous marker of tumor hypoxia. Eur J Nucl Med Mol Imaging 31:1530–1538
34. Lewis JS, McCarthy DW, McCarthy TJ, Fujibayashi Y, Welch MJ (1999) Evaluation of ^{64}Cu-ATSM *in vitro* and *in vivo* in a hypoxic tumor model. J Nucl Med 40:177–183
35. Piert M, Machulla HJ, Picchio M et al (2005) Hypoxia-specific tumor imaging with ^{18}F-fluoroazomycin arabinoside. J Nucl Med 46:106–113
36. Dakshinamurti K, Chauhan J, Ebrahim H (1987) Intestinal absorption of biotin and biocytin in the rat. Biosci Rep 7:667–673
37. Hainsworth J, Harrison P, Mather SJ (2005) Preparation and characterization of a DOTA–lysine–biotin conjugate as an effector molecule for pretargeted radionuclide therapy. Bioconjug Chem 16:1468–1474

Eur J Nucl Med Mol Imaging (2010) 37:1566–1574
DOI 10.1007/s00259-010-1467-4

ORIGINAL ARTICLE

Rapid detection of hypoxia-inducible factor-1-active tumours: pretargeted imaging with a protein degrading in a mechanism similar to hypoxia-inducible factor-1α

Masashi Ueda · Takashi Kudo · Yuji Kuge · Takahiro Mukai · Shotaro Tanaka · Hiroaki Konishi · Azusa Miyano · Masahiro Ono · Shinae Kizaka-Kondoh · Masahiro Hiraoka · Hideo Saji

Received: 8 December 2009 / Accepted: 29 March 2010 / Published online: 29 April 2010

Abstract
Purpose Hypoxia-inducible factor-1 (HIF-1) plays an important role in malignant tumour progression. For the imaging of HIF-1-active tumours, we previously developed a protein, POS, which is effectively delivered to and selectively stabilized in HIF-1-active cells, and a radioiodinated biotin derivative, (3-^{123}I-iodobenzoyl)norbiotinamide (^{123}I-IBB), which can bind to the streptavidin moiety of POS. In this study, we aimed to investigate the feasibility of the pretargeting method using POS and ^{123}I-IBB for rapid imaging of HIF-1-active tumours.
Methods Tumour-implanted mice were pretargeted with POS. After 24 h, ^{125}I-IBB was administered and subsequently, the biodistribution of radioactivity was investigated at several time points. In vivo planar imaging, comparison between ^{125}I-IBB accumulation and HIF-1 transcriptional activity, and autoradiography were performed at 6 h after the administration of ^{125}I-IBB. The same sections that were used in autoradiographic analysis were subjected to HIF-1α immunohistochemistry.
Results ^{125}I-IBB accumulation was observed in tumours of mice pretargeted with POS (1.6%ID/g at 6 h). This result is comparable to the data derived from ^{125}I-IBB-conjugated POS-treated mice (1.4%ID/g at 24 h). In vivo planar imaging provided clear tumour images. The tumoral accumulation of ^{125}I-IBB significantly correlated with HIF-1-dependent luciferase bioluminescence (R=0.84, p<0.01). The intratumoral distribution of ^{125}I-IBB was heterogeneous and was significantly correlated with HIF-1α-positive regions (R=0.58, p<0.0001).
Conclusion POS pretargeting with ^{123}I-IBB is a useful technique in the rapid imaging and detection of HIF-1-active regions in tumours.

Keywords Tumour hypoxia · Hypoxia-inducible factor-1 (HIF-1) · Oxygen-dependent degradation (ODD) · Molecular imaging · Pretargeting

M. Ueda
Radioisotopes Research Laboratory, Kyoto University Hospital, Faculty of Medicine, Kyoto University,
54 Shogoin Kawahara-cho, Sakyo-ku,
Kyoto 606-8507, Japan

M. Ueda · T. Kudo · Y. Kuge · H. Konishi · A. Miyano · M. Ono · H. Saji (✉)
Department of Patho-Functional Bioanalysis,
Graduate School of Pharmaceutical Sciences, Kyoto University,
46-29 Yoshida Shimoadachi-cho, Sakyo-ku,
Kyoto 606-8501, Japan
e-mail: hsaji@pharm.kyoto-u.ac.jp

Y. Kuge
Central Institute of Isotope Science, Hokkaido University,
Kita 15, Nishi 7, Kita-ku,
Sapporo 060-0815, Japan

T. Mukai
Department of Biomolecular Recognition Chemistry,
Graduate School of Pharmaceutical Sciences, Kyushu University,
3-1-1 Maidashi, Higashi-ku,
Fukuoka 812-8582, Japan

S. Tanaka · S. Kizaka-Kondoh · M. Hiraoka
Department of Radiation Oncology and Image-applied Therapy,
Graduate School of Medicine, Kyoto University,
54 Shogoin Kawahara-cho, Sakyo-ku,
Kyoto 606-8507, Japan

Introduction

Insufficient blood supply to a rapidly growing tumour leads to the presence of an oxygen tension below physiological

levels, i.e. hypoxia, in solid tumours [1]. Tumour hypoxia is critically important in tumour physiology and cancer treatment, and it appears to be strongly associated with malignant progression and therapy resistance. The transcription factor, hypoxia-inducible factor-1 (HIF-1) is induced in hypoxic regions. It is a master regulator of the genes that encode for angiogenic and metastatic factors, and plays an important role in tumour progression [2–4]. Thus, noninvasive imaging of HIF-1-active regions in tumours would be useful for characterizing tumours and determining a course of therapy.

HIF-1 is a heterodimer that consists of an oxygen-sensitive alpha subunit (HIF-1α) and a constitutively expressed beta subunit. In normoxia, two proline residues in the oxygen-dependent degradation (ODD) domain of HIF-1α are hydroxylated, leading to a proteasomal degradation of HIF-1α. Under hypoxic conditions, oxygen is the rate-limiting factor for prolyl hydroxylation, resulting in a decreased degradation of HIF-1α [5, 6]. That is to say, the ODD domain of HIF-1α is responsible for the regulation of HIF-1 activity. Thus, it is likely that a probe containing the ODD domain and degrading in a manner similar to HIF-1α could be used to evaluate HIF-1 activity in vivo.

We have recently developed proteins in which the protein transduction domain (PTD) is fused to the ODD domain and demonstrated the specificity of these proteins to HIF-1-active cells [7–11]. In a previous study, we also fused the PTD-ODD with a monomeric streptavidin (SAV) to produce a chimeric protein, PTD-ODD-SAV (POS); we also synthesized a radiolabelled biotin derivative, (3-$^{123/125}$I-iodobenzoyl)norbiotinamide ($^{123/125}$I-IBB). For nuclear medical imaging, the two were conjugated to give $^{123/125}$I-IPOS, the characterization of which has been presented previously [9]. In brief, POS was degraded in an oxygen-dependent manner and a clear tumour image was obtained 24 h after injection of ^{123}I-IPOS. In addition, the tumoral accumulation correlated with HIF-1 activity and the intratumoral distribution of ^{125}I-IPOS was heterogeneous and corresponded to hypoxic areas. These findings suggested that ^{123}I-IPOS is a potential probe for the imaging of HIF-1-active tumours. However, due to its large molecular size, ^{123}I-IPOS cleared from the blood slowly; thus, we could not obtain a high tumour-to-normal tissue ratio within a short time after probe injection.

To overcome this problem, we propose a pretargeting method based on the high-affinity interaction between SAV and biotin [12]. This method uses a combination of tumour-seeking molecules and the prompt clearance of low-molecular-weight radiolabelled compounds (effector molecules) that are cleared within minutes from the blood. One of the advantages of the pretargeting method is that it provides a high tumour-to-normal tissue ratio within a short time after injection. In addition, because the effector molecules used in this method are rapidly cleared from the body, radiation exposure is reduced. Moreover, some recent studies have shown that the tumour uptake of the effector molecules used in the pretargeting method is identical to or even higher than that of directly radiolabelled antibody. The images and therapeutic effects shown in these studies were significantly improved [13–15]. In the present study, we aimed to reveal the effectiveness of the pretargeting method using POS and ^{123}I-IBB in the rapid imaging of HIF-1-active tumour hypoxia.

Materials and methods

Cells and cell culture

FM3A mouse mammary tumour cells were purchased from Health Science Research Resources Bank (Osaka, Japan) and were cultured in 10% fetal bovine serum/RPMI-1640 medium (Nissui Pharmaceutical, Tokyo, Japan). Suit2 human pancreatic tumour cells that express luciferase in response to HIF-1 activity (Suit2/Luc cells) were established by Prof. Kizaka-Kondoh [16]. These cells were authenticated by s multiplex PCR method using short tandem repeat and were maintained in 10% fetal bovine serum/Dulbecco's modified Eagle's medium (Nissui Pharmaceutical). The culture media were supplemented with penicillin (100 U/ml) and streptomycin (100 μg/ml). Cells were incubated at 37°C in a well-humidified incubator with 5% CO_2 and 95% air.

Preparation of fusion protein

POS was overexpressed in *Escherichia coli* and purified as described in a previous report [9]. Purified POS was then dissolved in Tris-HCl buffer (pH 8.0).

Synthesis

Ammonium ^{123}I-iodide was kindly provided by Nihon Medi-Physics (Hyogo, Japan). Sodium ^{125}I-iodide was purchased from PerkinElmer Life and Analytical Sciences (Boston, MA). All other chemicals used in this study were of reagent grade and are commercially available. $^{123/125}$I-IBB and nonradioactive IBB were synthesized as described in a previous report [9, 17]. ^{123}I-IPOS was obtained by incubating ^{123}I-IBB and POS for 1 h, followed by purification on Sephadex G50 columns (GE Healthcare Bioscience, Uppsala, Sweden).

Animal model

Animal studies were conducted in accordance with our institutional guidelines, and the experimental procedures